

Beyond mean-field dynamics of small Bose-Hubbard systems based on the number-conserving phase space approach

F. Trimborn,^{1,2} D. Witthaut,^{1,3,*} and H. J. Korsch¹

¹*Fachbereich Physik, Technische Universität Kaiserslautern, D-67653 Kaiserslautern, Germany*

²*Institut für mathematische Physik, TU Braunschweig, D-38106 Braunschweig, Germany*

³*QUANTOP, Niels Bohr Institute, University of Copenhagen, DK-2100 Copenhagen, Denmark*

(Dated: May 29, 2018)

The number-conserving quantum phase space description of the Bose-Hubbard model is discussed for the illustrative case of two and three modes, as well as the generalization of the two-mode case to an open quantum system. The phase-space description based on generalized $SU(M)$ coherent states yields a Liouvillian flow in the macroscopic limit, which can be efficiently simulated using Monte Carlo methods even for large systems. We show that this description clearly goes beyond the common mean-field limit. In particular it resolves well-known problems where the common mean-field approach fails, like the description of dynamical instabilities and chaotic dynamics. Moreover, it provides a valuable tool for a semi-classical approximation of many interesting quantities, which depend on higher moments of the quantum state and are therefore not accessible within the common approach. As a prominent example, we analyse the depletion and heating of the condensate. A comparison to methods ignoring the fixed particle number shows that in this case artificial number fluctuations lead to ambiguities and large deviations even for quite simple examples.

PACS numbers: 03.75.Lm, 03.65.-w

I. INTRODUCTION

The physics of ultracold atoms in optical lattices has made an enormous progress in the last decade, since it is an excellent model system for a variety of fields such as nonlinear dynamics or condensed matter physics. The dynamics of bosonic atoms can be described by the celebrated Bose-Hubbard Hamiltonian, which is a paradigmatic model for the study of strongly correlated many-body quantum systems [1]. Such systems are hard to deal with theoretically since the dimension of the respective Hilbert space increases exponentially both in the particle number and in the number of lattice sites. Therefore, approximations to the dynamics are of considerable interest.

However, things can become surprisingly simple if the atoms undergo Bose-Einstein condensation. In many situations, the mesoscopic dynamics of a Bose-Einstein condensate (BEC) is extremely well described by the (discrete) Gross-Pitaevskii equation (GPE) for the macroscopic wavefunction of the condensate (see, e.g., [2]). This mean-field description is often referred to as 'classical' since the macroscopic limit $N \rightarrow \infty$ of the dynamics in second quantization is formally equivalent to the limit $\hbar \rightarrow 0$ which yields classical mechanics as the limit of single particle quantum mechanics. In practice, this approximation is frequently derived within a Bogoliubov approach, factorizing the expectation values of products of operators into the product of expectation values. As a consequence there is no obvious indicator to quantify the errors or to specify the scope of validity. Moreover, many

interesting observables which involve higher moments of quantum state are not accessible within this approximation. A more detailed overview over established methods and a comparison to the approach presented here will be given in Sec. VII.

The phase space formulation of quantum mechanics is nearly as old as the theory itself and has a wide range of applications, especially in quantum optics. Beneath the illustrative insight into the dynamics provided by this formulation, many techniques and methods were developed in this context. However, only a small fraction of the literature is dedicated to systems with intrinsic symmetries like the Bose-Hubbard Hamiltonian. In this case the dynamical group is isomorphic to the special unitary group $SU(M)$, with M being the number of lattice sites, reflecting the conservation of the total particle number. A general algorithm to construct phase space distribution functions for systems whose dynamical group has the structure of an arbitrary Lie group such as $SU(M)$ has been developed only nine years ago [3]. It is based on the concept of generalized coherent states introduced by Gilmore [4] and Perelomov [5]. Starting from these states we have surveyed the mathematical foundations of the number conserving phase space description and derived the exact evolution equations for the Husimi Q -function and the Glauber-Sudarshan P -function of the M -site Bose-Hubbard model in a preceding paper [6]. One important consequence of the use of $SU(M)$ coherent states is the different topology of the phase space, which is now isomorphic to the $2M - 2$ dimensional Bloch sphere and therefore compact. Moreover, the phase space description based on $SU(M)$ coherent states allows for a deeper analysis of the many-particle-mean-field correspondence, since these states are of high physical significance. As they are equivalent to the fully condensed

*Electronic address: dirk.witthaut@nbi.dk

product states, they provide an excellent tool to describe and study derivations from the macroscopic state which also determine the region validity of the mean-field approximation.

In this paper we will illustrate the methods originally developed for the M -site system [6] for the instructive case of small Bose-Hubbard systems. Therefore we consider a two-mode Bose Hubbard model

$$\hat{H} = -\Delta(t) \left(\hat{a}_1^\dagger \hat{a}_2 + \hat{a}_2^\dagger \hat{a}_1 \right) + \epsilon_2 \hat{a}_2^\dagger \hat{a}_2 + \epsilon_1 \hat{a}_1^\dagger \hat{a}_1 + \frac{U}{2} \left(\hat{a}_1^{\dagger 2} \hat{a}_1^2 + \hat{a}_2^{\dagger 2} \hat{a}_2^2 \right), \quad (1)$$

and its generalization which takes into account elastic collisions with background gas leading to phase noise described by a master equation. Such a system can be realized experimentally by confining a BEC in a double-well trap [7, 8, 9, 10]. Moreover, we also consider the case of an explicitly time-dependent tunneling-element Δ , which leads to mixed regular-chaotic mean-field dynamics. This can be easily implemented in an experimental setup via a variation of the intensity of the laser forming the optical potential. However, this model can also describe the fundamental phenomena of two weakly coupled BECs in more general setups [11] and Landau-Zener transitions between different Bloch bands [12, 13]. Early theoretical studies of the system dynamics without an external influence and a time-dependant driving were reported in [14, 15, 16]. Furthermore, we use the methods presented here to analyse the interesting and yet not completely understood case $M = 3$, i.e. the three-mode Bose-Hubbard system:

$$\hat{H} = -\Delta_{12} \left(\hat{a}_1^\dagger \hat{a}_2 + \hat{a}_2^\dagger \hat{a}_1 \right) - \Delta_{23} \left(\hat{a}_2^\dagger \hat{a}_3 + \hat{a}_3^\dagger \hat{a}_2 \right) + \sum_{j=1}^3 \epsilon_j \hat{a}_j^\dagger \hat{a}_j + \frac{U}{2} \sum_{j=1}^3 \hat{a}_j^{\dagger 2} \hat{a}_j^2. \quad (2)$$

The realization of such a linear triple-well trap for a BEC is not as straightforward as in the case of a double-well trap, but nevertheless possible in optical setups [17] or on an atom-chip. Besides it is a prominent model system because the mean-field dynamics is classically chaotic (see, e.g. [18, 19, 20, 21]).

In particular, this paper is organised as follows: In the sections II and III, we briefly recall the main results from the number conserving phase space approach and provide some illustrative examples. Then follows an analysis of the exact dynamics of the quasi probability distributions in Sec. IV. Here, we are especially interested in the macroscopic limit, since the evolution equations converge to a classical Liouville equation for large particle numbers. This result enables us to go beyond the usual mean-field limit which considers only point-distributions and to enhance the region of applicability of the approximation to arbitrary initial states. To emphasize this, we study in Sec. V the behaviour around dynamical instabilities where the common mean-field approach is known to

fail badly. In the case of an isolated instability this effect is known as the breakdown of mean-field. Here, we show that the Liouville dynamics not only resolves this breakdown due to an isolated instability, but also provides an ideal tool to describe systems where the mean-field dynamics faces large chaotic regions, as for example in a driven two mode system.

Having demonstrated the considerable advantages of the Liouville description, we are now able to address novel questions, like the dynamics of the three-mode system in Sec. VI. While being conceptually quite simple and much easier to implement than other methods (cf. e.g. [22, 23]) the Liouville description provides a valuable tool to estimate the depletion of the condensate mode and to infer the nature of the many-body quantum state. The comparison to exact numerical results show clear agreement with the results of the Liouville equation while the common mean-field approach fails.

Since the methods developed in [6] are not restricted to the Bose-Hubbard model, but can be applied to every problem within the same symmetry group, there is a large variety of possible applications. As one example, we discuss the heating of a two-mode BEC resulting from elastic scattering with the background gas in Sec. VI C. While our methods predict the proper results, namely a quasi-classical set of Langevin equations in the mean-field approximation, they allow to go even further and predict many interesting effects such as the decay of the coherence factor and the increase of the variances, which are not accessible within the usual mean-field limit. This again underlines the benefit from the Liouville description and the distinction to common mean-field approaches.

In Sec. VII we then give a short overview over different approaches to derive and extend a mean-field description for the systems studied here. Especially, we compare our approach based on the dynamical symmetry and therefore explicitly including the conservation of the particle number to common phase space methods (cf. e.g. [24, 25]). One important result is that calculations based on a $U(1)$ symmetry breaking description using common Glauber coherent states show deviations from the exact dynamics which are significantly larger and appear on a shorter time scale compared to the number conserving approach.

II. ALGEBRAIC STRUCTURE AND GENERALIZED COHERENT STATES

The number conserving phase space description of the Bose-Hubbard dynamics has been introduced in [6], starting from the generalized coherent states of Gilmore [4] and Perelomov [5]. Here we will only recall the main results for the special case of two and three modes for the sake of completeness.

Generalized coherent states for arbitrary dynamical Lie groups are defined by the action of a translation

operator onto a reference state. For instance, the celebrated Glauber coherent states for the Heisenberg-Weyl group H_4 are defined by the relation $|\alpha\rangle = \hat{D}(\alpha)|0\rangle = e^{\alpha\hat{a}^\dagger - \alpha^*\hat{a}}|0\rangle$, where the reference state is just the vacuum state. The parameter space of the translation operators $\hat{D}(\alpha)$ and thus the space of the coherent states is isomorphic to the classical phase space $\mathbb{C} \simeq \mathbb{R} \times \mathbb{R}$.

A. The two-mode case

The situation is different for a BEC in a double well trap since the dynamical group is now $SU(2)$ spanned by the angular momentum operators

$$\begin{aligned}\hat{J}_x &= \frac{1}{2}(\hat{a}_1^\dagger\hat{a}_2 + \hat{a}_2^\dagger\hat{a}_1), \\ \hat{J}_y &= \frac{i}{2}(\hat{a}_1^\dagger\hat{a}_2 - \hat{a}_2^\dagger\hat{a}_1), \\ \hat{J}_z &= \frac{1}{2}(\hat{a}_2^\dagger\hat{a}_2 - \hat{a}_1^\dagger\hat{a}_1).\end{aligned}\quad (3)$$

The Hamiltonian (1) then can be rewritten as

$$\hat{H} = -2\Delta\hat{J}_x + 2\epsilon\hat{J}_z + U\hat{J}_z^2 \quad (4)$$

with $\epsilon = \epsilon_2 - \epsilon_1$ up to a constant term [14, 15, 26, 55]. The Casimir operator $\hat{J}^2 = \hat{N}/2(\hat{N}/2 + 1)$ reveals the relation between the algebraic structure and the total particle number $\hat{N} = \hat{a}_1^\dagger\hat{a}_1 + \hat{a}_2^\dagger\hat{a}_2$.

Generalization of the concept of the translation operator to the $su(2)$ algebra yields an rotation operator, such that the $SU(2)$ or so called Bloch coherent states are defined as follows:

$$\begin{aligned}|\theta, \phi\rangle &= \hat{R}(\theta, \phi)|N, 0\rangle \\ &= e^{-i\theta(\hat{J}_x \sin\phi - \hat{J}_y \cos\phi)}|N, 0\rangle \\ &= \sum_{n_1+n_2=N} \binom{N}{n_2}^{\frac{1}{2}} \cos\left(\frac{\theta}{2}\right)^{n_1} \sin\left(\frac{\theta}{2}\right)^{n_2} e^{-in_2\phi}|n_1, n_2\rangle.\end{aligned}\quad (5)$$

The group of rotations $\hat{R}(\theta, \phi)$ and therefore the parameter space of coherent states can be described by two angles $0 \leq \theta \leq \pi, 0 \leq \phi < 2\pi$ and is thus isomorphic to a Bloch sphere \mathcal{S}^2 . In physical terms, this can be understood as follows: The z -component of the Bloch vector describes the population imbalance of the two modes, while the polar angle represents the relative phase. Since this variable is cyclic and not defined if all particles are in a single well (i.e. at the poles), the topology is clearly that of a sphere.

Note that the $SU(M)$ coherent states are equivalent to the product states, i.e. they represent a pure condensate [6, 27] For two modes, $M = 2$, this relation simply reads

$$|\theta, \phi\rangle = \frac{1}{\sqrt{N!}} \left(\cos\left(\frac{\theta}{2}\right)a_1^\dagger + \sin\left(\frac{\theta}{2}\right)e^{-i\phi}a_2^\dagger \right)^N |0, 0\rangle. \quad (6)$$

This representation of $SU(2)$ coherent states reveals a parametrization in more physical terms p, q , where $q = \phi$

is equal to the relative phase between the modes and $p = \cos^2(\theta/2)$ denotes the population of the second mode.

B. The three-mode case

For the three-mode system the dynamical group is isomorphic to $SU(3)$ which is spanned by the eight generators

$$\begin{aligned}\hat{X}_1 &= \hat{a}_1^\dagger\hat{a}_1 - \hat{a}_2^\dagger\hat{a}_2, \\ \hat{X}_2 &= \frac{1}{3}(\hat{a}_1^\dagger\hat{a}_1 + \hat{a}_2^\dagger\hat{a}_2 - 2\hat{a}_3^\dagger\hat{a}_3), \\ \hat{Y}_k &= i(\hat{a}_k^\dagger\hat{a}_j - \hat{a}_j^\dagger\hat{a}_k), \\ \hat{Z}_k &= \hat{a}_k^\dagger\hat{a}_j + \hat{a}_j^\dagger\hat{a}_k,\end{aligned}\quad (7)$$

with $k = 1, 2, 3$ and $j = k + 1 \pmod{3}$, which form a generalized angular momentum algebra (cf. e.g. [6, 28]).

A convenient choice of basis is given by the eigenstates of the Casimiroperator $4\hat{N}(\hat{N}/3+1)$ with $\hat{N} = \sum_{i=1}^3 \hat{a}_i^\dagger\hat{a}_i$ and the two elements of the Cartan subalgebra \hat{X}_1 and \hat{X}_2 with

$$\hat{n}_k|n_1, n_2, n_3 = N - n_1 - n_2\rangle = n_k|n_1, n_2, n_3\rangle. \quad (8)$$

In this basis the reference state is chosen to be the highest weight state $|N, 0, 0\rangle$ and the generalized coherent states $|\Omega\rangle$ are obtained by the natural extension of (5) to higher dimensional rotations. Note, that $SU(3)$ is a two instead of one parameter Lie group, thus the parameter space of generalized the coherent states is now isomorphic to $SU(3)/U(2)$ and therefore four-dimensional. In order to visualize the phase space dynamics we must hence use projections and Poincaré sections, which are not necessarily be unique. For further mathematical details, see e.g. [28] for $SU(3)$, as well as [6, 29] for the general case $SU(M)$.

However, for any actual calculation or numerical simulation the equivalent parametrization of the generalized coherent states $|\Omega\rangle$ via the complex mode amplitudes ψ_i

$$|\Omega\rangle = \frac{1}{\sqrt{N!}} \left(\sum_{i=1}^3 \psi_i \hat{a}_i^\dagger \right)^N |0, 0, 0\rangle \quad (9)$$

proves to be more practical. Using the conservation of the total particle number which corresponds to the normalization $\|\psi\|^2 = |\psi_1|^2 + |\psi_2|^2 + |\psi_3|^2 = 1$, we can fully characterize the state vector by the occupations $p_2 = |\psi_2|^2$, $p_3 = |\psi_3|^2$ and the relative phases $q_1 = \arg(\psi_2) - \arg(\psi_1)$ and $q_3 = \arg(\psi_2) - \arg(\psi_3)$, as discussed in the case of the two mode system. Therefore we will use this parametrization in the following.

Note, that such a description in terms of $SU(3)$ coherent states has already proven useful in the case of a circular arrangement with uniform tunneling elements $\Delta_{ij} = \Delta = \text{const.}$ [30] and in the study of quantum discrete vortices [31]. A comparison of these results to calculations based on common Glauber coherent states can be found in [32].

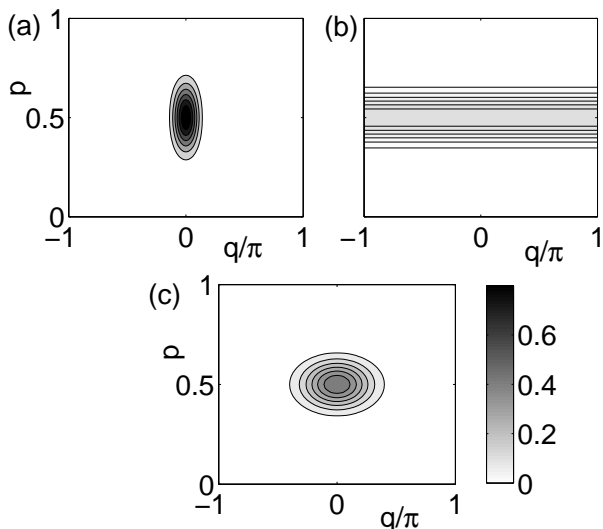


FIG. 1: Husimi functions in a Mercator projection of (a) the coherent state $|p = 1/2, q = 0\rangle$, (b) the Fock state $|n_1 = N/2, n_2 = N/2\rangle$ and (c) the ground state of the Hamiltonian (1) for $\Delta = 1$, $U = 10$ and $\epsilon = 0$. The number of particles is $N = 40$ in all plots.

III. PHASE SPACE DISTRIBUTIONS

With the help of the generalized coherent states, which will be denoted $|\Omega\rangle$ in the following (independently of the corresponding dynamical group), one can readily introduce quasi phase space distributions for a BEC in a double or triple well trap. The Glauber-Sudarshan P -distribution is defined as the diagonal representation of the density operator $\hat{\rho}$ in generalized coherent states

$$\hat{\rho} = \int_X P(\Omega) |\Omega\rangle \langle \Omega| d\mu(\Omega), \quad (10)$$

where Ω represents the respective parametrization and $d\mu(\Omega)$ stands for the invariant measure on the respective phase space, denoted by X . Due to the overcompleteness of the coherent states, the P -function does always exist but is usually not unique. Furthermore it is not positive definite and often highly singular. On the other hand, the Husimi Q -function defined as the expectation value of the density operator in generalized coherent states,

$$Q(\Omega) = \langle \Omega | \hat{\rho} | \Omega \rangle, \quad (11)$$

is unique, regular and positive definite. Thus the Q -function is especially suited for illustrations, while both quasi distribution functions will be used for actual calculations. However, the Q -function is also not a probability distribution function in the strict sense since it does not give the correct marginal distributions. Note that it is also possible to define the Wigner function on a spherical phase space but this leads to much more complicated expressions than the P - and Q -function, since its construction uses harmonic functions on the respective phase space. This makes actual calculations a hard

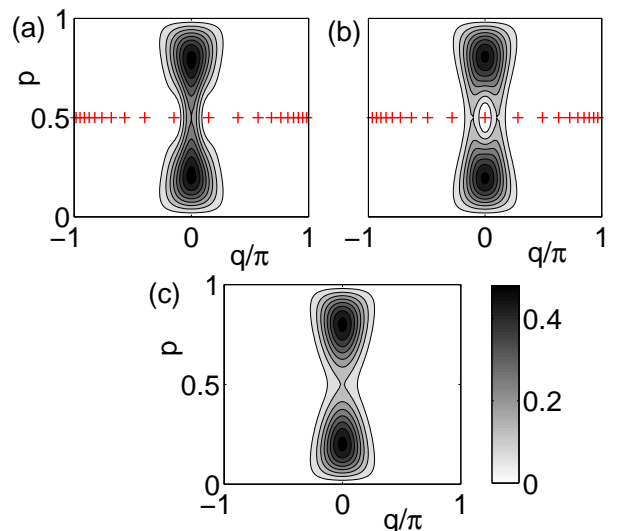


FIG. 2: (Color online) Husimi density of the cat states $|\psi_{\pm}\rangle \propto |0.2, 0\rangle \pm |0.8, 0\rangle$ (a),(b) and the incoherent sum $\hat{\rho}_+ = (|0.2, 0\rangle \langle 0.2, 0| + |0.8, 0\rangle \langle 0.8, 0|)/2$ (c) for $N = 20$ particles. The zeros of the Husimi function are marked by red crosses.

task even for two lattice sites corresponding to $SU(2)$ (see, e.g., the contradictory results in [33] and [34]) and almost impossible for larger systems. Furthermore, a positive P -representation respecting $SU(M)$ symmetry has been introduced and analyzed in [35].

To get a first impression of the phase space distributions considered here we have plotted the Husimi function of the two mode system for (a) the coherent state $|p = 1/2, q = 0\rangle$, (b) the Fock state $|n_1 = N/2, n_2 = N/2\rangle$ and (c) the ground state of the Hamiltonian (1) for $\Delta = 1$ and $U = 10$ in a Mercator projection of the sphere in Fig. 1. The coherent state is maximally localized at the position (p, q) and thus closest to a point in classical phase space. On the contrary a Fock state is localized around $p = n_2/N$. The phase q is completely delocalized in the sense that the Husimi function is uniform in q . Finally one can clearly visualize the number squeezing of the eigenstate (c) in comparison with the coherent state (a) due to the interaction term in the Hamiltonian – a fact which is desirable for matter wave interferometer experiments [36].

The overcompleteness of the basis of (generalized) coherent states guarantees that one can uniquely reconstruct the quantum state out of the quasi probability distribution. It is even possible to determine a pure state solely from the N zeros of the Husimi function or the Bargmann function up to a global phase factor [37]. Thus these zeros carry the essential information about the quantum state and its coherence properties. As an example, Fig. 2 compares the Husimi distribution of a cat state in the two mode case, i.e. a coherent superposition of two $SU(2)$ coherent states $|\psi_{\pm}\rangle \propto |p = 0.2, q = 0\rangle \pm |p = 0.8, q = 0\rangle$, with the incoherent sum of

these two states $\hat{\rho}_+ = (|0.2, 0\rangle\langle 0.2, 0| + |0.8, 0\rangle\langle 0.8, 0|)/2$. The global shape of the Husimi function of the three states appears quite similar with significant differences only around the point $(p, q) = (0.5, 0)$. The Husimi density is increased for the coherent superpositions $|\psi_+\rangle$ in (a) and decreased for $|\psi_-\rangle$ in (b) in comparison with the incoherent sum, reflecting constructive or destructive interference, respectively. The complete information about the pure states $|\psi_\pm\rangle$ is coded in the distribution of the $N = 20$ zeros of the Husimi function, which are plotted as red crosses in the figure. The Husimi function of the mixed state $\hat{\rho}_+$ has no zero at all, whereas the Husimi function of a coherent state (compare also Fig. 1) has a single N -fold degenerate zero opposite to the maximum of the quasi probability distribution.

IV. DYNAMICS AND THE MACROSCOPIC LIMIT

Evolution equations for the classical phase space distributions can be derived using the mapping of operators in Hilbert space to differential operators on the classical phase space. The \mathcal{D}^ℓ -algebra representation of an arbitrary hermitian operator \hat{A} is defined such that the resulting differential operator acting on the parametrization of the generalized coherent state projector has exactly the same effect as the original operator:

$$\hat{A}|\Omega\rangle\langle\Omega| \stackrel{!}{=} \mathcal{D}^\ell(\hat{A})|\Omega\rangle\langle\Omega|, \quad (12)$$

$$|\Omega\rangle\langle\Omega|\hat{A} \stackrel{!}{=} \mathcal{D}^\ell(\hat{A})^*|\Omega\rangle\langle\Omega|. \quad (13)$$

Here, the superscript ℓ refers to side (left) from which the operator acts. The \mathcal{D}^ℓ -algebra representation is well known for the Heisenberg-Weyl algebra. It has been introduced for the $su(M)$ -algebra by Gilmore and coworkers (see [4] and references therein). Here, we just state the expression for the generators of the $su(2)$ -algebra in the angular parametrization (5):

$$\begin{aligned} \mathcal{D}^\ell(\hat{L}_+) &= e^{i\phi} \left(\frac{N}{2} \sin\theta + \frac{i}{2} \cot\frac{\theta}{2} \frac{\partial}{\partial\phi} + \cos^2\frac{\theta}{2} \frac{\partial}{\partial\theta} \right), \\ \mathcal{D}^\ell(\hat{L}_-) &= e^{-i\phi} \left(\frac{N}{2} \sin\theta - \frac{i}{2} \tan\frac{\theta}{2} \frac{\partial}{\partial\phi} - \sin^2\frac{\theta}{2} \frac{\partial}{\partial\theta} \right), \\ \mathcal{D}^\ell(\hat{L}_z) &= -\frac{N}{2} \cos\theta + \frac{1}{2} \sin\theta \frac{\partial}{\partial\theta} + \frac{i}{2} \frac{\partial}{\partial\phi}. \end{aligned} \quad (14)$$

Independently of the number of modes M , the evolution equation for the Q -function can be expressed in terms of the differential operators \mathcal{D}^ℓ :

$$\begin{aligned} \frac{\partial}{\partial t} Q(\Omega) &= \text{tr}(\dot{\hat{\rho}}|\Omega\rangle\langle\Omega|) \\ &= -i \text{tr}(\hat{\rho}\hat{H}|\Omega\rangle\langle\Omega| - |\Omega\rangle\langle\Omega|\hat{H}\hat{\rho}) \quad (15) \\ &= -i(\mathcal{D}^\ell(\hat{H}) - \mathcal{D}^\ell(\hat{H})^*)Q(\Omega). \end{aligned}$$

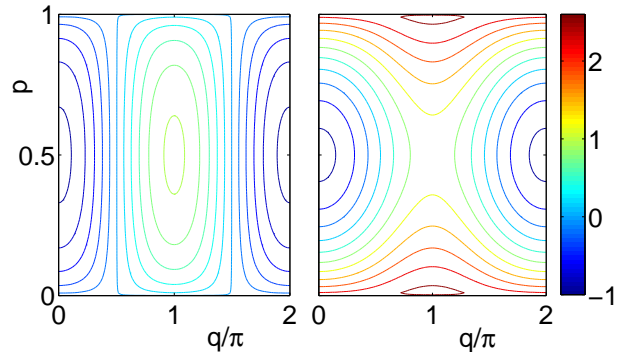


FIG. 3: (Color online) Classical phase space structure: Lines of constant energy $\mathcal{H}(p, q)$ for $\Delta = 1$, $\epsilon = 0$, and $g = 0$ (left) resp. $g = 10$ (right).

For the P -function we need an associated $\tilde{\mathcal{D}}^\ell$ -algebra defined by an integration by parts:

$$\begin{aligned} \int_X \{P(\Omega)\mathcal{D}^\ell(H)\}|\Omega\rangle\langle\Omega| d\mu(\Omega) &= \\ \int_X \{\tilde{\mathcal{D}}^\ell(H)P(\Omega)\}|\Omega\rangle\langle\Omega| d\mu(\Omega). \end{aligned} \quad (16)$$

Using this algebra, the evolution equation for the P -function can be derived via

$$\begin{aligned} \dot{\hat{\rho}} &= \int_X \frac{\partial}{\partial t} P(\Omega)|\Omega\rangle\langle\Omega| d\mu(\Omega) = \\ &= \int_X i \left(\tilde{\mathcal{D}}^\ell(H) - \tilde{\mathcal{D}}^\ell(H)^* \right) P(\Omega)|\Omega\rangle\langle\Omega| d\mu(\Omega). \end{aligned} \quad (17)$$

The \mathcal{D}^ℓ -algebra representation of the relevant operators and the evolution equation for the M -site Bose-Hubbard-Hamiltonian have been calculated in the preceding paper [6]. They are generally applicable to every problem within this symmetry class.

A. Mean-field dynamics of the two-mode system

Since the mapping to the differential operators is linear, the explicit evolution equations for the Q - and P -function can be directly calculated from the imaginary part (cf. Eqn. (15) and (17)) of the \mathcal{D}^ℓ operators (see Eqn. (14)). This yields the following results:

$$\begin{aligned} \frac{\partial}{\partial t} Q(p, q) &= \left\{ +2\epsilon \frac{\partial}{\partial q} \right. \\ &+ \Delta \left(2\sqrt{p-p^2} \sin q \frac{\partial}{\partial p} + \frac{1-2p}{\sqrt{p-p^2}} \cos q \frac{\partial}{\partial q} \right) \\ &\left. + U \left(N(1-2p) - 2p(1-p) \frac{\partial}{\partial p} \right) \frac{\partial}{\partial q} \right\} Q(p, q) \end{aligned} \quad (18)$$

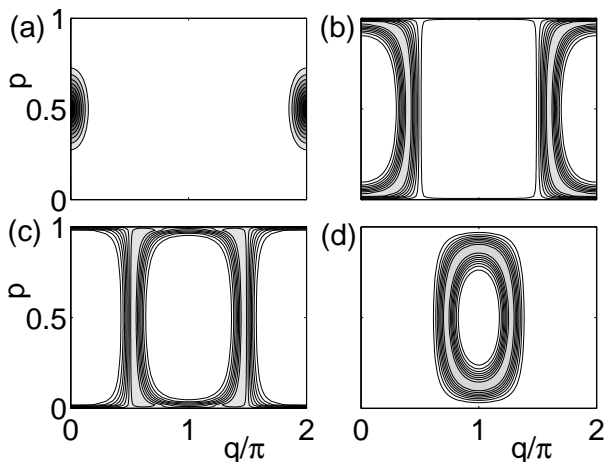


FIG. 4: Husimi density of the eigenstates $|E_n\rangle$ with $n = 1, 15, 23, 34$ (a-d) of the Hamiltonian (1) for $\Delta = 1$, $\epsilon = 0$, $UN = 0$ and $N = 40$ particles. Dark colors encode high values of the Husimi density.

for the Husimi Q -function and

$$\begin{aligned} \frac{\partial}{\partial t} P(p, q) = & \left\{ +2\epsilon \frac{\partial}{\partial q} \right. \\ & + \Delta \left(2\sqrt{p-p^2} \sin q \frac{\partial}{\partial p} + \frac{1-2p}{\sqrt{p-p^2}} \cos q \frac{\partial}{\partial q} \right) \\ & \left. + U \left((N+2)(1-2p) + 2p(1-p) \frac{\partial}{\partial p} \right) \frac{\partial}{\partial q} \right\} P(p, q) \end{aligned} \quad (19)$$

for the Glauber-Sudarshan P -function.

One can directly show that both evolution equations conserve the normalization. Furthermore it can be shown that the interaction terms $\sim U$ cancel exactly for $N = 1$, since a single Boson obviously does not interact. The expectation values of the angular momentum operators (3) are exactly given by the phase space averages [6]

$$\begin{aligned} \langle \hat{J}_k \rangle &= (N+2) \int_{\mathcal{S}^2} s_k(p, q) Q(p, q) d\mu(p, q) \quad \text{and} \\ \langle \hat{J}_k \rangle &= N \int_{\mathcal{S}^2} s_k(p, q) P(p, q) d\mu(p, q), \end{aligned} \quad (20)$$

where $k = x, y, z$ and

$$\mathbf{s} = \begin{pmatrix} \sqrt{p(1-p)} \cos(q) \\ \sqrt{p(1-p)} \sin(q) \\ p - 1/2 \end{pmatrix} \quad (21)$$

is the classical Bloch vector.

These exact equations provide a valuable starting point to study the limit of large particle numbers, since it emerges quite naturally in the phase space picture. In the macroscopic limit $N \rightarrow \infty$ with $g = UN$ fixed, the second order derivative terms in the evolution equations become negligible, as they are vanishing as $\mathcal{O}(1/N)$. The appearance of a non-positive diffusion term as the difference between the exact quantum dynamics and the classical dynamics has already been discussed in [38]. Thus, in

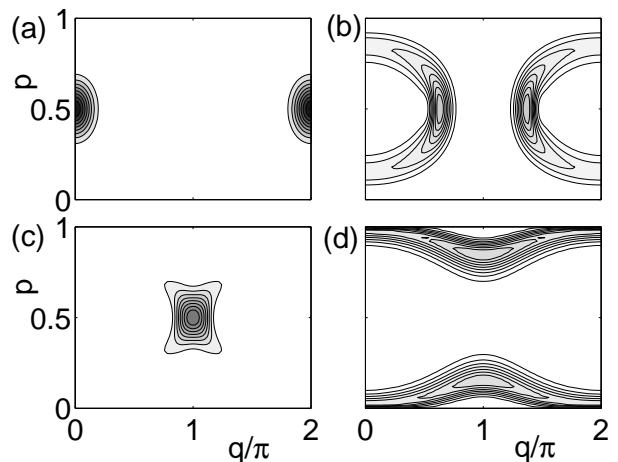


FIG. 5: As Fig. 4, however for $UN = 10$.

the macroscopic case one obtains a Liouville equation for a quasi-classical phase space distribution function $\rho(p, q)$:

$$\begin{aligned} \frac{\partial}{\partial t} \rho(p, q) &= - \left(\frac{\partial \mathcal{H}}{\partial p} \frac{\partial}{\partial q} - \frac{\partial \mathcal{H}}{\partial q} \frac{\partial}{\partial p} \right) \rho(p, q) \\ &= - \{ \mathcal{H}(p, q), \rho(p, q) \} \end{aligned} \quad (22)$$

with the Poisson bracket $\{\cdot, \cdot\}$ and the Gross-Pitaevskii Hamiltonian function

$$\mathcal{H} = -2\epsilon p - 2\Delta \sqrt{p(1-p)} \cos(q) + \frac{g}{4} (1-2p)^2. \quad (23)$$

The macroscopic interaction strength depends upon the operator ordering and is thus given by $g = UN$ if we start from the Q -function and by $\tilde{g} = U(N+2)$ for the P -function. This difference also vanishes in the macroscopic limit $N \rightarrow \infty$ with $g = UN$ fixed. Therefore the phase space picture gives rise to a Liouvillian flow for the time-evolution of the quasi probability distribution in the macroscopic limit.

The common mean-field limit is subject to even more severe restrictions. To circumstantiate this point, we will have a closer look at the relation between the Liouville dynamics and the GPE. To obtain the latter, one must not only take the macroscopic limit of the evolution equations (18) and (19), but also assume a pure condensate, respectively a $SU(M)$ coherent state which is maximally localized during the whole time evolution. In this case the dynamics of a phase the space distribution of the initial state is approximated by a point distribution, respective a single trajectory instead of an extended distribution. Therefore, any information about quantities involving higher moments of the state is lost.

So, if we assume a delta-distribution $\rho(p', q') = \delta(p' - p) \delta(q' - q)$, we can derive the GPE starting from the Liouville equation (22). This yields the canonical equations

of motion

$$\begin{aligned}\dot{p} &= -\frac{\partial \mathcal{H}}{\partial q} = -2\Delta \sqrt{p(1-p)} \sin(q) \\ \dot{q} &= \frac{\partial \mathcal{H}}{\partial p} = -2\epsilon - \Delta \frac{1-2p}{\sqrt{p(1-p)}} \cos(q) - g(1-2p).\end{aligned}\quad (24)$$

These equations are equivalent to the celebrated discrete Gross-Pitaevskii equation

$$i \frac{d}{dt} \begin{pmatrix} \psi_1 \\ \psi_2 \end{pmatrix} = \begin{pmatrix} \epsilon + g|\psi_2|^2 & -\Delta \\ -\Delta & -\epsilon + g|\psi_1|^2 \end{pmatrix} \begin{pmatrix} \psi_1 \\ \psi_2 \end{pmatrix}, \quad (25)$$

if one identifies $\psi_1 = \sqrt{1-p}$ and $\psi_2 = \sqrt{p} \exp(-iq)$ and neglects the global phase. In the non-interacting case $U = 0$, these mean-field equations of motion are exact and an initially coherent state remains coherent in time. Hence, no information is lost, since the higher moments can be easily reconstructed. However, in the interacting case an initially pure BEC typically deviates quite rapidly from the set of maximally localized states. Moreover, by approximating the state by a product state one loses the entire information about the higher moments of the state. Therefore many quantities of interest as for example variances etc. are not accessible, whereas they can be easily estimated using the Liouville dynamics and phase space averages similar to Eqn. (20).

The classical phase space structure induced by the Hamiltonian function (23) is shown in Fig. 3 for $\Delta = 1$, $\epsilon = 0$ and two different value of the interaction strength, $g = 0$ and $g = 10$. In the linear case one recovers the simple Rabi or Josephson oscillations. One of the elliptic fixed points bifurcates if the interaction strength exceeds the critical value $g = 2\Delta$, leading to the self-trapping effect [14, 15, 16].

Furthermore, we have plotted the Husimi function for some selected eigenstates of the Bose-Hubbard Hamiltonian (1) for the linear case $UN = 0$ in Fig. 4 and for $UN = 10$ in Fig. 5. The Husimi functions of the eigenstates localize on the classical phase space trajectories of the respective energy as shown in Fig. 3, where their sum covers the classical phase space uniformly,

$$\sum_n Q_{|n\rangle}(p, q) = 1. \quad (26)$$

In the linear case $UN = 0$, the classical trajectories correspond to the Josephson oscillations between the two wells as shown on the left-hand side of Fig. 3. This behavior is directly mirrored by the eigenstates as shown in Fig. 4: The lowest eigenstate localizes on the classical fixed point $(p, q) = (0, 0)$ while the others correspond to Josephson oscillations.

The situation is more interesting, when the interaction strength exceeds the critical value for the self-trapping bifurcation, as shown exemplarily for $UN = 10$ in Fig. 5. For low energies one still finds Rabi modes, while the eigenstates of higher energies correspond to self-trapping trajectories with a persistent particle number difference

and a running phase (cf. Fig. 3, right). However, the eigenstates always localize equally on the trajectories with $p > 1/2$ and $p < 1/2$ because of the symmetry of the Hamiltonian (4). Most interestingly, quantum states can also localize at the unstable hyperbolic fixed point as shown in Fig. 5 (c).

B. Mean-field dynamics of the three-mode system

As in the case of the two-mode system, the exact evolution equations of the phase space distribution functions can be calculated from the \mathcal{D}^ℓ operators. The results given in [6] are considerably more complicated as in the case of only two modes. However, in the macroscopic limit one again recovers a Liouville equation

$$\frac{\partial}{\partial t} \rho(p_1, p_3, q_1, q_3) = -\{\mathcal{H}, \rho(p_1, p_3, q_1, q_3)\} \quad (27)$$

with the macroscopic Hamiltonian function

$$\begin{aligned}\mathcal{H} &= \epsilon_1 p_1 + \epsilon_3 p_3 + \frac{g}{2} (p_1^2 + p_3^2 + (1-p_1-p_3)^2) \\ &\quad - 2\Delta_{12} \sqrt{1-p_1-p_3} \sqrt{p_1} \cos(q_1) \\ &\quad - 2\Delta_{23} \sqrt{1-p_1-p_3} \sqrt{p_3} \cos(q_3).\end{aligned}\quad (28)$$

The main new feature of the dynamics in three-levels systems is that the mean-field dynamics can become classically chaotic (cf. e.g. [18, 19, 20, 21] and references therein), where the transition goes from regular dynamics for $g = 0$, to mixed chaotic dynamics for stronger nonlinearities $|g|$, whereas the mean-field dynamics of the two mode system with constant parameters is always regular. Figure 6 (a) shows a Poincaré section of the corresponding phase space for $g = -5$ and $\mathcal{H} = 1$, where the dynamics is still mostly regular. However, a classically chaotic strip is found between the elliptic fixed point at $(p_3, q_3) = (0.66, 0)$ and the running phase modes below. Chains of large regular islands are found within this chaotic sea (colored in green in the figure). Another example is shown in Fig. 6 (b) for $g = -10$ and $\mathcal{H} = -1$. Again we observe elliptic fixed points with large values of p_3 separated from the running phase modes by a chaotic region in phase space. However, the regular running phase modes now occupy most of the energetically allowed region of phase space. Furthermore one observes a novel fixed point embedded in this region of phase space.

This phase space structure is typical for the route to chaos in Hamiltonian systems described by the KAM and the Poincaré-Birkhoff theorem. The dynamics becomes chaotic in the phase space region close to the separatrix. Resonant tori are destroyed and decompose into a series of elliptic and hyperbolic fixed points, where the elliptic ones form the island chains embedded in the chaotic region. The remaining invariant tori confine this chaotic sea.

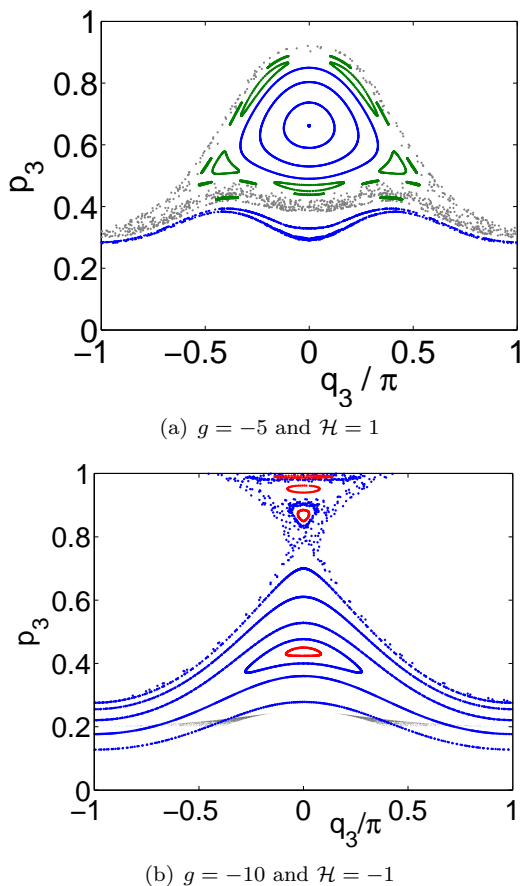


FIG. 6: (Color online) Poincaré section of the classical phase space ($q_1 = 0$, see text for details) for $\epsilon_1 = 2$, $\epsilon_3 = 4$, $\Delta_{12} = \Delta_{23} = 1$, $g = -5$ and a fixed total energy $\mathcal{H} = +1$ (a) and $-g = 10$ and $\mathcal{H} = -1$ (b). Trajectories around the elliptic fixed points are coloured in red to guide the eye.

Note that the use of a Poincaré section is not straightforward for the dynamical system considered here. As usual, the variables (p_3, q_3) are plotted when the trajectories intersect the $q_1 = 0$ -plane with $\dot{q}_1 > 0$. The remaining dynamical variable p_1 follows from energy conservation. However the uniqueness has to be checked explicitly. For example, the assignment of p_1 is not unique in Fig. 6 (b) in a small area of phase space which is shaded in grey in the figure. Solving equation (28) for p_1 gives two possible solutions. In order to make the calculation of p_1 unique we define that only the solution with smaller value of p_1 is plotted in the Poincaré section. Furthermore, large regions of the (p_3, q_3) -plane are energetically forbidden for $q_1 = 0$ (cf. Fig. 6).

Let us have a closer look at the mixed classically-chaotic phase space shown in Fig. 6 (b). The dynamics is also shown in a three-dimensional phase space plot in Fig. 7. Only few trajectories are plotted exemplarily. The periodic orbits (coloured in red) correspond to the elliptic fixed points in the Poincaré section (Fig. 6). Two periodic orbits are found on the left-hand side of the figure, oscillating with a small amplitude both in the

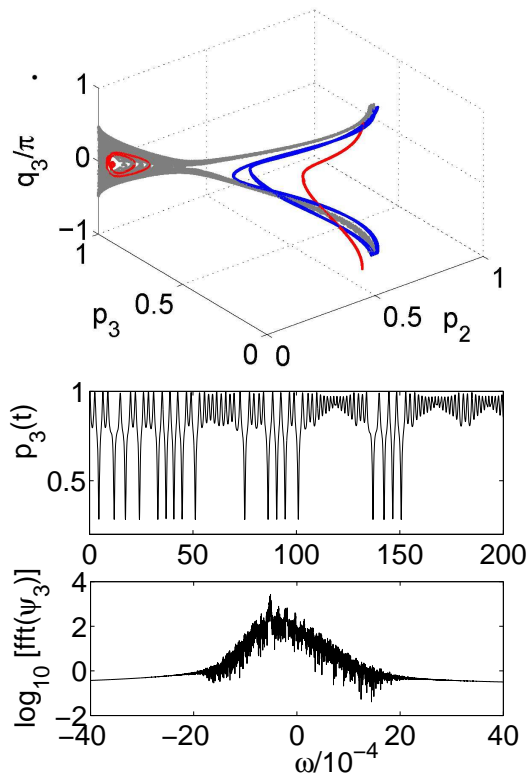


FIG. 7: (Color online) Upper panel: mean-field phase space trajectories for $\epsilon_1 = 2$, $\epsilon_3 = 4$, $\Delta_{12} = \Delta_{23} = 1$, $g = -10$ and a fixed total energy $\mathcal{H} = -1$. Lower panel: Time series ($p_3(t) = |\psi_3(t)|^2$) and power spectrum of a trajectory in the chaotic sea.

populations and in the relative phases. Another periodic trajectory shows a larger amplitude of the oscillations of the populations p_2 and p_3 and a running phase q_3 . This periodic trajectory is embedded in a set of similar quasi-periodic ones, of whom one is plotted as a blue line in the figure. Furthermore, a trajectory in the chaotic sea is plotted in grey. It is observed that the chaotic sea splits into two distinct regions with narrow links: One around the periodic orbits on the left and one in the vicinity of the running-phase trajectory on the right-hand side.

This 'bottleneck' effect leads to an intermittent dynamics: A trajectory can be confined to certain regions in the chaotic sea for a long time, where its time evolution looks quasi regular. Chaotic bursts to the remaining part of the chaotic sea are found between the quasi-regular oscillations. This is shown in Fig. 7, where the time series $p_3(t)$ for one particular trajectory in the chaotic sea is plotted as well as the corresponding power spectrum. One observes long quasi-regular oscillations with a small amplitude intermittent by large amplitude bursts. Physically this means that the BEC mostly stays in the right well for a long time with irregular bursts to the middle well.

In conclusion, we stress that in any case, two steps of approximation were necessary to derive the Gross-

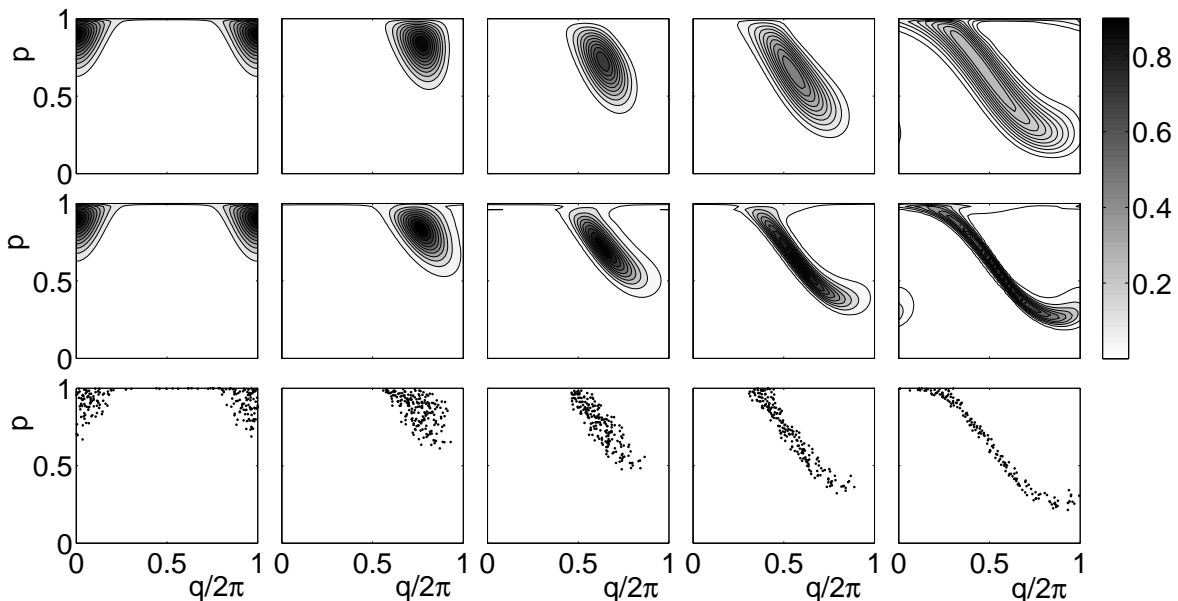


FIG. 8: Breakdown of the mean-field approximation around a hyperbolic fixed point in phase space. Shown is the dynamics of an initially coherent state located at $p_0 = 0.9045$ and $q_0 = 0$ at times $t = 0, 0.12, 0.24, 0.36, 0.48$ (from left to right) for $\Delta = 1$, $UN = 10$ and $N = 20$ particles. The exact quantum evolution of the Husimi function (top) is compared to the classical Liouvillean dynamics (middle) and to the dynamics of a classical phase space ensemble (bottom).

Pitaevskii equation: In the first step we have neglected the quantum noise term in the evolution equations (18) and (19) which is always possible in the macroscopic limit $N \rightarrow \infty$ with $g \equiv UN$ fixed. Only in the second step to derive the GPE one assumes a nearly pure condensate, so that its phase space representation is strongly localized and can be approximated by a point distribution or a single trajectory in phase space.

Thus it is not only possible to simulate the dynamics of a strongly localized product state, but also of every other possible initial state using the Liouville equation while the error vanishes as $1/N$. Whereas the single-trajectory mean-field approximation will break down if the quantum state differs significantly from a product state, the phase space description still gives excellent results. This issue and its implications will be further investigated in the following.

V. ANALYSIS OF DYNAMICAL INSTABILITIES AND CHAOS

The phase-space description of the Bose-Hubbard model is especially suited to explore the correspondence of the quasi-classical mean-field approximation and the many-particle quantum dynamics. The established derivations of the Gross-Pitaevskii equation assume a fully coherent quantum state, so that the mean-field approximation is restricted to this class of quantum states. In fact it has been shown that the approximation is no longer valid if the Gross-Pitaevskii dynamics becomes classically unstable [22, 23]. In this section, we inves-

tigate the behaviour of the mean-field approximation around localized, as well as extended regions of dynamical instabilities. It is shown, that the Liouville dynamics not only resolves well-known problems of the common mean-field description, but enables us to even study highly chaotic systems.

A. Resolution of the break-down of mean-field

A particular illustrative example of the failure of the common mean-field equations was introduced by Anglin and Vardi [26, 39], who demonstrated the breakdown of the mean-field approximation for a two-mode BEC around the hyperbolic fixed point shown in Fig. 3 on the right-hand side. Therefore, this is an excellent example to demonstrate that the approximation by the Liouville dynamics clearly goes beyond the usual mean-field description and to enlighten the reason of the break-down. The top row of Fig. 8 shows the resulting evolution of the quantum Husimi Q -function. Initially the system is in a fully condensed state, i.e. a $SU(2)$ coherent state at $p_0 = 0.9045$ and $q_0 = 0$, and thus the Husimi function is maximally localized. In the course of time the condensate approaches the hyperbolic fixed point, where the Husimi function rapidly diffuses along the unstable classical manifold. The coherence is lost and the Gross-Pitaevskii equation is no longer valid. This is further illustrated in Fig. 9, where the evolution of the quantum Bloch vector $\langle \hat{\mathbf{J}} \rangle / N$ (solid blue line) is compared to its classical counterpart \mathbf{s} (solid red line). Both agree well in the beginning, when the system is fully condensed. How-

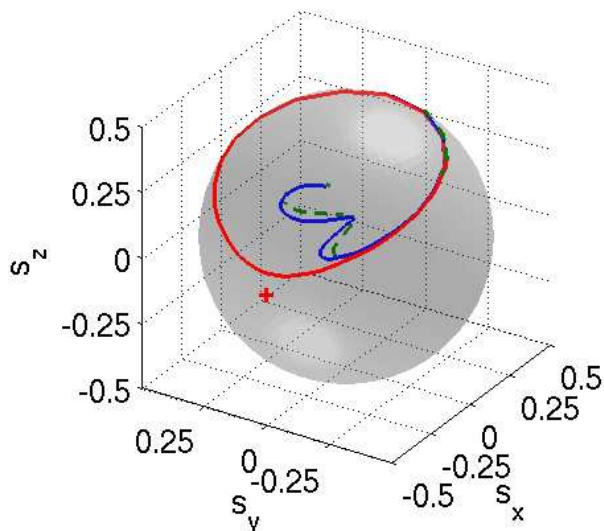


FIG. 9: (Color online) Time evolution of the Bloch vector $\langle \hat{\mathbf{J}} \rangle / N$ approaching the hyperbolic fixed point (solid blue line) for the same parameters as in Fig. 8. The ensemble average over 500 trajectories (dashed green line) closely follows the quantum result, while a single trajectory (solid red line) breaks away in the vicinity of the hyperbolic fixed point (marked by a cross).

ever, the mean-field approximation breaks down as they approach the hyperbolic fixed point (marked by a cross in the figure). The quantum Bloch vector penetrates into the Bloch sphere, while the classical vector \mathbf{s} is restricted to the surface.

However, this breakdown of the mean-field approximation is only due to the neglect of higher moments of the quantum state and not a consequence of a failure of the quasi-classical Gross-Pitaevskii dynamics. Thus it is easily resolved in quantum phase space. The middle row of Fig. 8 shows the evolution of a classical phase space distribution propagated by the Liouville equation (22) which coincides with the Husimi function at $t = 0$. With increasing particle number N the width of the initial distribution decreases such that one recovers a single phase space point in the macroscopic limit $N \rightarrow \infty$. One observes that the classical distribution captures the essential features of the quantum evolution – the spreading along the unstable manifold of the hyperbolic fixed point. Due to the neglect of the second order differential term in Eqn. (18) this spreading is a little overestimated while the quantum spreading in the orthogonal direction is absent. Thus, this can be construed as a disregard of quantum noise which guarantees the uncertainty relation. Furthermore we can interpret the Liouvillian flow in terms of a classical phase space ensemble as shown in the bottom row of Fig. 8. At $t = 0$ this ensemble is generated by 500 phase space points to mimic the quantum Husimi distribution. Afterwards all trajectories evolve according to the Gross-Pitaevskii equation (25) resp. (24). This approximation is comparable to nu-

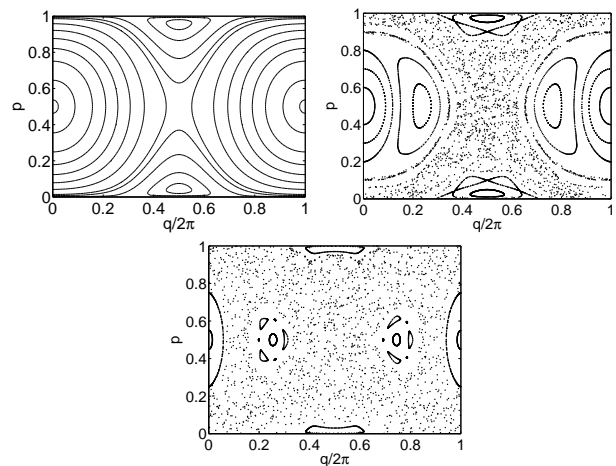


FIG. 10: Stroboscopic Poincaré section of the classical dynamics of a driven two-mode BEC for $\Delta_0 = 1$, $g = 5$, $\omega = 2\pi$ and $\Delta_1 = 0, 0.2, 0.5$ (from top left to bottom).

merical Monte Carlo methods and especially suited for the generalization to larger systems, since it is easily implementable. Fig. 9 shows the quasi-classical expectation value of the Bloch vector (dashed green line) calculated by the simple phase space average (20) in comparison to the quantum Bloch vector $\langle \hat{\mathbf{J}} \rangle / N$. One observes an excellent agreement. Note that the expectation values calculated from the classical distribution function and the phase space ensemble are indistinguishable on this scale and thus only one curve is shown in the figure.

B. Description of chaos in a driven two-mode system

Periodically driven Bose-Hubbard systems are of current interest (see, e.g., [40] and references therein). In this paragraph, we consider the dynamics in a double-well trap for a time-dependent tunneling matrix element

$$\Delta(t) = \Delta_0 + \Delta_1 \cos(\omega t). \quad (29)$$

Such a driving can be implemented easily in an optical setup by varying the intensity of the laser beams forming the optical lattice. Figure 10 shows a stroboscopic Poincaré section of the mean-field dynamics for the parameters $\Delta_0 = 1$, $g = 5$, $\Delta_1 = 0, 0.2, 0.5$ and $\omega = 2\pi$ so that the period is $T = 1$. The fixed points of the stroboscopic mapping correspond to the nonlinear Floquet solutions of the driven GPE (cf. also [40]). For $\Delta_1 = 0$ one obviously recovers the undriven system, which is completely regular. A mixed regular-chaotic dynamics is found when Δ_1 is increased, the region around the hyperbolic fixed point $(p, q) = (1/2, \pi)$ being the first to become chaotic. Fig. 10 (b) shows the phase space for $\Delta_1 = 0.5$, where only tiny regular islands have survived, among them regions around the symmetric fixed point $(p, q) = (1/2, 0)$ and the self-trapping fixed

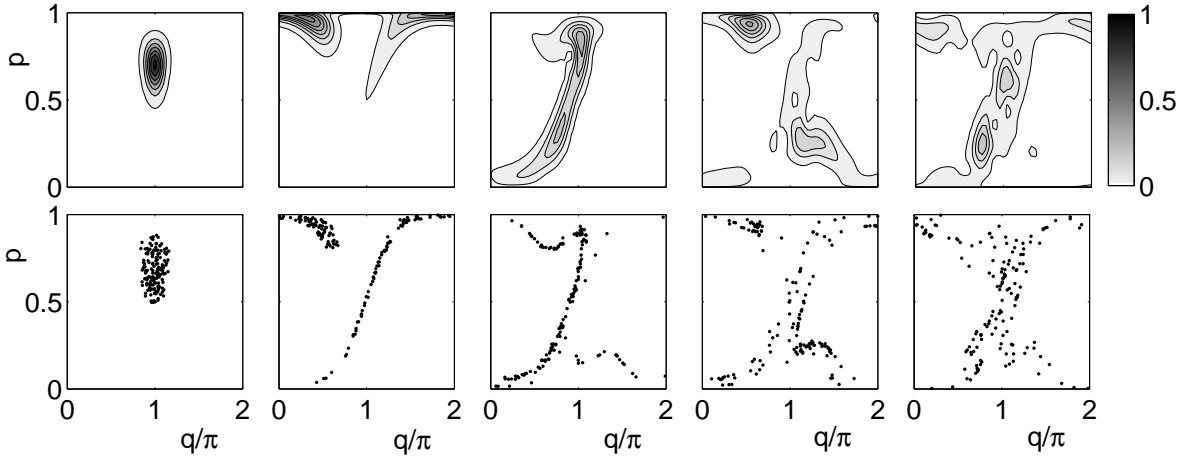


FIG. 11: Comparison of quantum and classical dynamics in phase space in the chaotic sea for $UN = 5$, $\Delta_0 = 1$, $\omega = 2\pi$ and $\Delta_1 = 0.5$ and $N = 20$ particles. Upper panels: Exact Evolution of the Husimi density at times $t = 0, 1, 2, 3, 4$ (from left to right). Lower panels: Dynamics of an ensemble of 150 classical trajectories.

points. The regular islands around $(p, q) = (1/2, \pi/2)$ and $(p, q) = (1/2, 3\pi/2)$ correspond to a period doubled fixed point. They are of particular interest since they support regular oscillations of the population with an extremely large amplitude as illustrated in Fig. 12.

If the classical dynamics is unstable, an initially coherent quantum state will be strongly distorted. For an isolated unstable fixed point, the state spreads along the unstable manifold while it is squeezed in the orthogonal direction as shown in Fig. 8. This makes the standard mean-field approximation fail, but may even be desirable [41]. Classical chaos has a much more dramatic effect: An initial coherent state will rapidly spread over the entire chaotic sea. Thus, the description by a sharply peaked distribution instantaneously fails and the Bogoliubov approach breaks down immediately. Again this breakdown is resolved by the introduction of a phase space ensemble as shown in Fig. 11. The classical ensemble well describes the spreading of the wave packet in the chaotic sea, demonstrating the power of the phase space approach also for classically chaotic dynamics.

The differences between regular and chaotic classical dynamics is furthermore illustrated in Fig. 12, where we have plotted the dynamics of the population in the second well $\langle \hat{n}_2(t) \rangle / N$ and the magnitude of the Bloch vector $|\langle \hat{\mathbf{J}}(t) \rangle| / N$ for two different initial states. The figures compare the exact many-particle dynamics (solid blue line) to the results of an ensemble simulation (dashed green line), showing a very good agreement for both regular and chaotic dynamics. If the initial state is located on an island as in Fig. 12 (a) and (b), the population imbalance oscillates regularly and the magnitude of the Bloch vector remains close to its maximum value $|\langle \hat{\mathbf{J}} \rangle| = N/2$. In this example we have chosen an initial state localized on a period-double fixed point (cf. Fig. 10), so that the population difference oscillates with only half of the driving period. The dynamics of a state initially localized in

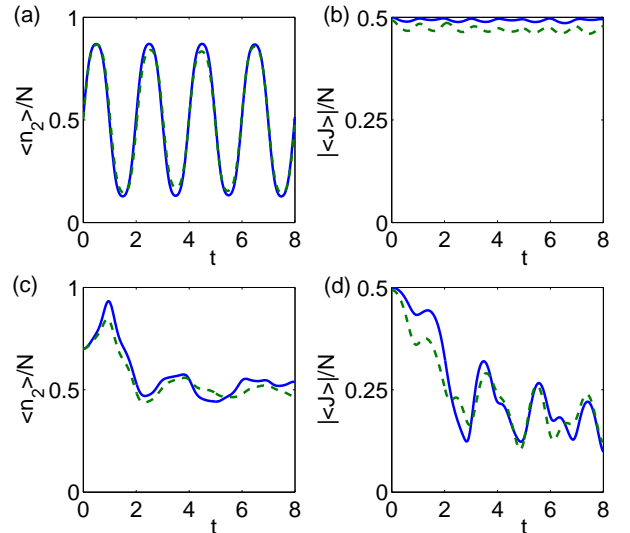


FIG. 12: (Color online) Quantum dynamics in a driven double-well trap for an initially coherent state localized at $(p, q) = (1/2, 3\pi/2)$ on a regular island (a),(b) and localized at $(p, q) = (0.7, 0)$ in the chaotic sea (c),(d). The population in the second well $\langle \hat{n}_2(t) \rangle / N$ is plotted on the left-hand side and the magnitude of the Bloch vector $|\langle \hat{\mathbf{J}}(t) \rangle| / N$ is plotted on the right-hand side, both calculated exactly (solid blue lines) and with a classical ensemble simulation (dashed green lines). The remaining parameters are $UN = 5$, $\Delta_0 = 1$, $\omega = 2\pi$, $\Delta_1 = 0.5$ and $N = 50$ particles.

the chaotic sea is shown Fig. 12 (c) and (d). Oscillations are rapidly damped out and the magnitude of the Bloch vector drops to very small values.

As mentioned above, the classical phase space structure does not only affect the quantum dynamics, but also the organization the eigenstates (cf. Sec. III). Due to the mixed phase space, this leads to much richer structures in

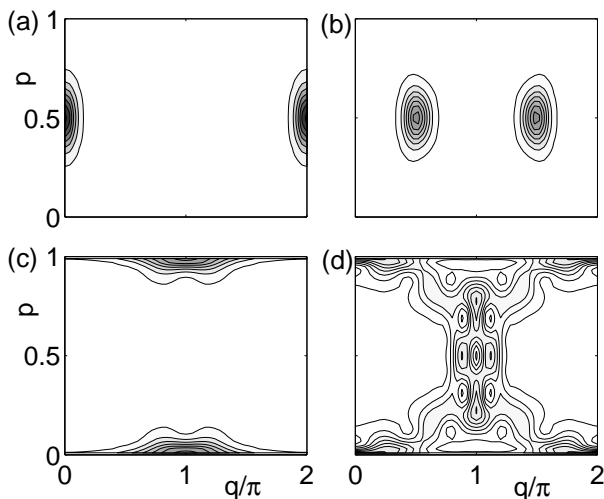


FIG. 13: Husimi representation of four typical Floquet states for a driven double-well trap with parameters $UN = 5$, $\Delta_0 = 1$, $\omega = 2\pi$, $\Delta_1 = 0.5$ and $N = 50$ particles.

the driven case. Instead of the eigenstates of the Hamiltonian, we now have to consider the Floquet states, which are defined as the eigenstates of the time evolution operator over one period T ,

$$\hat{U}(T) = \hat{\mathcal{T}} \exp \left(-i \int_0^T \hat{H}(t') dt' \right), \quad (30)$$

where $\hat{\mathcal{T}}$ is the time ordering operator. Figure 13 shows the Husimi representation of four typical Floquet states for $\Delta_1 = 0.5$. Three regular states are shown in the parts (a)–(c), corresponding to the symmetric, the self-trapping and the period-doubled fixed point, respectively. The period-doubled Floquet state shown in part (c) oscillates with a large amplitude during one driving period, in which it remains well localized. In contrast, the chaotic eigenstate are delocalized over the complete chaotic sea – a typical example is shown in part (d) of the figure.

VI. BEYOND MEAN-FIELD: DEPLETION AND HEATING OF THE CONDENSATE

In this section we show that the Liouville picture also provides an excellent quasi-classical approximation of many-particle quantities that are not accessible within the common single-trajectory mean-field description, since it also takes into account approximately the higher moments of the quantum state. In particular one can readily determine the deviation from a pure BEC and calculate the higher moments of the angular momentum operators (3) that can be used to quantify many-particle entanglement [41]. In this paragraph we will especially discuss the first issue for the two- and three-mode case in more detail. This is closely related to the preceding sections, as it is a clear signature of the regular and chaotic dynamics in the corresponding quantum system.

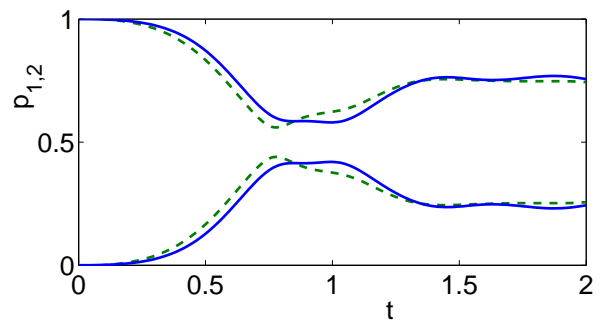


FIG. 14: (Color online) Eigenvalues of the reduced single-particle density matrix (31) calculated from the quantum (solid blue line) and the quasi-classical (dashed green line) Bloch vector depicted in Fig. 9.

However, the Liouville description is not restricted to standard Bose-Hubbard systems. Therefore, we consider the generalization of the two-mode system to an open system in the last paragraph of this section. Here, one quantity of particular interest is the coherence factor between the two modes which decreases during the heating process [9]. It is shown that the Liouville description provides a valuable approximation of this decoherence process.

A. The two-mode Bose-Hubbard system

The deviation from a pure BEC can be characterized by the eigenvalues of the reduced single-particle density matrix (SPDM)

$$\rho_{\text{red}} = \frac{1}{N} \begin{pmatrix} \langle \hat{a}_1^\dagger \hat{a}_1 \rangle & \langle \hat{a}_1^\dagger \hat{a}_2 \rangle \\ \langle \hat{a}_2^\dagger \hat{a}_1 \rangle & \langle \hat{a}_2^\dagger \hat{a}_2 \rangle \end{pmatrix}, \quad (31)$$

which are easily found to be given by

$$\lambda_{\pm} = \frac{1}{2} \pm \frac{|\langle \hat{\mathbf{J}} \rangle|}{N}. \quad (32)$$

The leading eigenvalue of the SPDM gives the condensate fraction, i.e. the relative population of the condensate mode [42]. Thus, a BEC is pure if this eigenvalue is equal to one, i.e. if the Bloch vector lies on the surface of the Bloch sphere, $|\langle \hat{\mathbf{J}} \rangle|/N = 1/2$. As discussed above, the expectation value of the angular momentum operators can be calculated from the quasi-classical phase space distribution function $\rho(p, q)$ in a good approximation. From these it is also possible to reconstruct the SPDM and its eigenvalues completely classically. Furthermore, it is important to note that these quantities are not accessible within a single trajectory mean-field approach, which always assumes a pure BEC and thus guarantees $|\langle \mathbf{s} \rangle| = 1/2 = \text{const}$. To illustrate our point further we compare the eigenvalues of the SPDM from the quasi-classical Liouville approximation with the exact quantum results in Fig. 14.

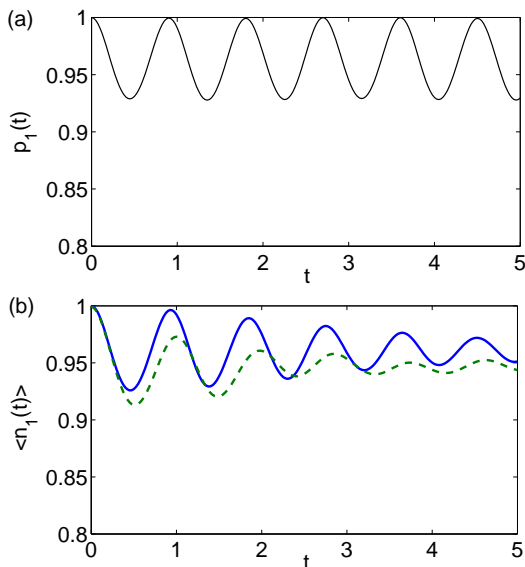


FIG. 15: (Color online) Classical and quantum dynamics in a three-mode system for an initial state in the regular region of classical phase space ($\psi_1(0) = 1$). The upper panel shows the occupation in the first well $p_1(t)$ calculated within the standard mean-field approximation. The lower panel shows the quantum expectation value $\langle \hat{n}_1(t) \rangle / N$ (solid blue line) and the ensemble expectation value (dashed green line). The parameters are $\epsilon_1 = 2$, $\epsilon_3 = 4$, $\Delta_{12} = \Delta_{23} = 1$, $UN = -10$ and $N = 80$ particles.

Initially one eigenvalue is unity, indicating a pure BEC equivalent to a product state with every particle in the same mode. This eigenvalue decreases rapidly when the Husimi function approaches the hyperbolic fixed point (cf. Fig. 8), indicating a rapid depletion of the condensate mode. One observes that the classical calculation reproduces this depletion of the condensate mode very well.

B. The three-mode Bose-Hubbard system

The same method can now be used to analyse the three-mode case. Two examples are shown in Figs. 15 and 16, where the standard mean-field approximation on the left-hand is compared to the results of a full quantum calculation and a classical ensemble simulation. The figures show the population in the first and the third mode, respectively. Regular oscillations with a small amplitude are found for an initial state localized in the first well ($\psi_1(0) = 1$, cf. Fig. 15). These oscillations are weakly damped in the quantum system due to a dephasing process. This damping is well reproduced by a classical ensemble calculations, while there is no damping at all in the standard mean-field approach (upper panel).

The dynamics is completely different for an initial state in the chaotic region of classical phase space as shown in Fig. 16. The upper panel shows the mean-field trajectory

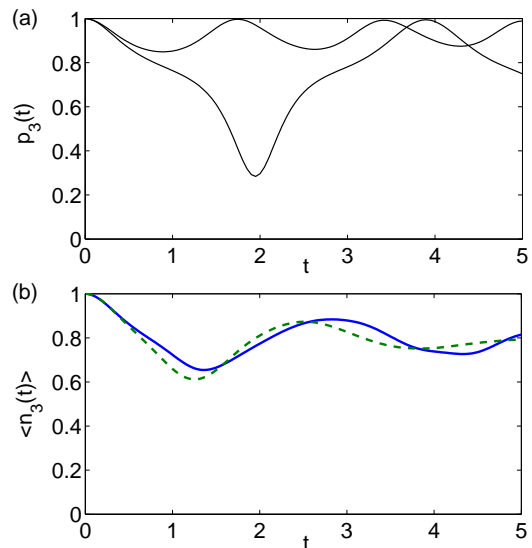


FIG. 16: (Color online) Classical and quantum dynamics in a three-mode system for an initial state in the chaotic region of classical phase space. The upper panel shows the occupation in the third well $p_3(t)$ calculated within the standard mean-field approximation for $p_3(0) = 1$ and $p_3(0) = 0.999$, respectively. The lower panel shows the quantum expectation value $\langle \hat{n}_3(t) \rangle / N$ (solid blue line) and the ensemble expectation value (dashed green line) for $\psi_3(0) = 1$. The parameters are $\epsilon_1 = 2$, $\epsilon_3 = 4$, $\Delta_{12} = \Delta_{23} = 1$, $UN = -10$ and $N = 80$ particles.

ries for two slightly different initial states ($p_3(0) = 1$ and $p_3(0) = 0.999$). They deviate fast and differ completely for $t \gtrsim 0.5$. The dynamics of the corresponding quantum system is shown in the lower panel for an initial state which is completely localized in the third mode,

$$|\Psi(0)\rangle = \frac{1}{\sqrt{N!}} (\hat{a}_3^\dagger)^N |0, 0, 0\rangle. \quad (33)$$

The oscillations of the density $\langle \hat{n}_3 \rangle$ are rapidly damped out. Again this is well reproduced by a classical ensemble calculation. In this case the only signature of chaos in the common mean-field description is the sensible dependence on the initial state, however again there is no indication of the damping process.

As we have already seen in the preceding paragraph, the ensemble simulation gives a good estimate of many-particle quantities, which cannot be calculated in the standard mean-field theory. Figure 17 shows the evolution of the eigenvalues of the SPDM, which is defined analogously to Eqn. (31) for the two-mode case. The results from a numerical solution of the many-particle dynamics are plotted as red lines, the ensemble estimates as dashed blue lines. The leading eigenvalues of the SPDM gives the condensate fraction of the many-particle quantum state. The condensate mode is depleted if the classical dynamics is unstable in favor of the remaining modes [22, 23, 26, 39]. The differences between the regular and chaotic case are obvious. As expected, the condensate

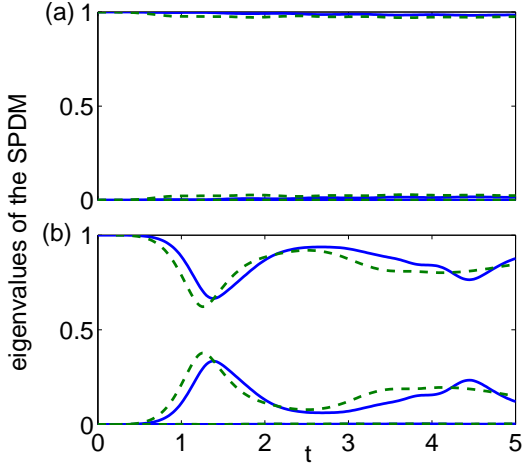


FIG. 17: (Color online) Evolution of the eigenvalues of the SPDM for (a) an initial state in the regular region of classical phase space ($\psi_1(0) = 1$) and (b) in the chaotic sea ($\psi_3(0) = 1$). Quantum results (blue solid lines) are compared to the classical ensemble estimate (dashed green lines). The parameters are chosen as in Fig. 15 and 16, respectively.

mode is significantly depleted if the dynamics is chaotic. The leading eigenvalue decreases fast, whereas it remains close to one if the dynamics is regular. Furthermore one observes a very good agreement of the classical and the quantum results. Therefore the ensemble method provides a valuable tool to estimate the depletion of the condensate mode and to infer the nature of the many-body quantum state from a purely classical calculation. This is especially useful for extended lattices, where quantum calculations become a hard problem. Another method to calculate the depletion of the condensate mode from the mean-field dynamics was introduced in [22, 23]. However, its use is technically more involved than the simple ensemble approach, while it gives no additional information.

C. Heating of a two-mode BEC

Recently, the long-time dynamics of a BEC interacting with the background gas has attracted a lot of interest [9, 43, 44, 45]. It was shown that collisions with the background gas lead to a decrease of the coherence of the two condensate modes, which can be used as a noise thermometer at extremely low temperatures. In this section we want to discuss the heating of a BEC within the quasi-classical phase space picture.

The main source of decoherence and heating is caused by elastic collisions with the background gas atoms and can be described in leading order by the master equation [46, 47]

$$\dot{\hat{\rho}} = -i[\hat{H}, \hat{\rho}] - \frac{\gamma_1}{2} \sum_{j=1,2} \hat{n}_j^2 \hat{\rho} + \hat{\rho} \hat{n}_j^2 - 2\hat{n}_j \hat{\rho} \hat{n}_j. \quad (34)$$

The latter term describes elastic scattering events that conserve the number of particles in the condensate mode and only lead to phase decoherence (see, e.g., [48]). Thus they are readily described within the number conserving phase space approach discussed in the present paper, where the interpretation as phase noise becomes especially clear.

The effects of the scattering events are conveniently understood and visualized in quantum phase space. The evolution equation for the Husimi function is obtained as in Sec. III by taking the expectation value in $SU(2)$ coherent states:

$$\begin{aligned} \frac{\partial}{\partial t} Q(p, q) &= \langle p, q | \dot{\hat{\rho}} | p, q \rangle \\ &= i \text{tr} \left(\hat{H} \hat{\rho} - \hat{\rho} \hat{H} | p, q \rangle \langle p, q | \right) \\ &\quad - \frac{\gamma_1}{2} \sum_{j=1,2} \text{tr} \left(\hat{n}_j^2 \hat{\rho} + \hat{\rho} \hat{n}_j^2 - 2\hat{n}_j \hat{\rho} \hat{n}_j | p, q \rangle \langle p, q | \right). \end{aligned} \quad (35)$$

Using the \mathcal{D}^ℓ -algebra representation of the operators introduced above, this equation can be cast into the form

$$\begin{aligned} \frac{\partial}{\partial t} Q(p, q) &= -2 \text{Im}(\mathcal{D}^\ell(\hat{H})) Q(p, q) \\ &\quad - \frac{\gamma_1}{2} \sum_{j=1,2} (\mathcal{D}^\ell(\hat{n}_j) - \mathcal{D}^\ell(\hat{n}_j)^*)^2 Q(p, q) \\ &= -\{\mathcal{H}(p, q), Q(p, q)\} \\ &\quad - 2Up(1-p) \frac{\partial^2}{\partial p \partial q} Q(p, q) + \gamma_1 \frac{\partial^2}{\partial q^2} Q(p, q), \end{aligned} \quad (36)$$

with the classical Hamiltonian function (23). By an analogous calculation one finds the evolution equation for the Glauber-Sudarshan distribution:

$$\begin{aligned} \frac{\partial}{\partial t} P(p, q) &= -\{\mathcal{H}(p, q), P(p, q)\} \\ &\quad + 2Up(1-p) \frac{\partial^2}{\partial p \partial q} P(p, q) + \gamma_1 \frac{\partial^2}{\partial q^2} P(p, q), \end{aligned} \quad (37)$$

keeping in mind that the macroscopic interaction strength is now given by $\tilde{g} = U(N+2)$ instead of $g = UN$. In these representations the effect of the decoherence term $\sim \gamma_1$ becomes most obvious: It leads to a diffusion of the relative phase of the two condensates and thus to a blurring of the coherence of the two condensates modes. This effect has been directly measured in the experiments of the Oberthaler group [9, 43].

If we neglect the quantum noise term $\sim g/N$, the equations (37) and (38) reduce to Fokker-Planck equations. Thus the condensate dynamics can again be interpreted in terms of phase space ensembles, now subject to the stochastic evolution equations

$$\dot{p} = -\frac{\partial \mathcal{H}}{\partial q} \quad \text{and} \quad \dot{q} = +\frac{\partial \mathcal{H}}{\partial p} + \sqrt{2\gamma_1} \xi(t), \quad (38)$$

where $\xi(t)$ describes uncorrelated white noise:

$$\langle \xi(t) \rangle = 0 \quad \text{and} \quad \langle \xi(t) \xi(t') \rangle = \delta(t - t'). \quad (39)$$

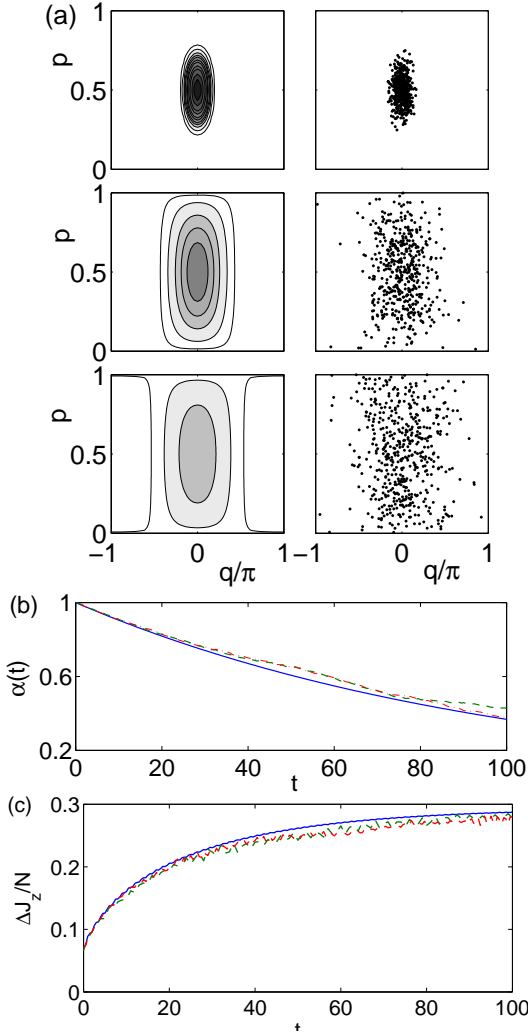


FIG. 18: (Color online) Heating of a two-mode BEC in quantum phase space for $UN = 0$, $\Delta = 1$, $\epsilon = 0$ and $\gamma_1 = 0.01$. (a) Comparison of the exact quantum evolution of the Husimi function $Q(p, q, t)$ (left-hand side) and the stochastic dynamics of a classical phase space ensemble (right-hand side) for $t = 0, 30, 60$ (from bottom to top). Dark colors encode high values of the Husimi density. (b) Decay of the coherence factor $\alpha(t)$. The exact quantum result (solid blue line) is compared to ensemble simulations based on the Q -function (dashed green line) and the P -function (dash-dotted red line).

An example for this quasi-classical description of phase diffusion due to heating of the condensate is shown in Fig. 18(a) for $UN = 0$ and Fig. 19(a) for $UN = 10$, respectively. The left hand side shows the exact quantum evolution of the Husimi distribution $Q(p, q, t)$ calculated from the evolution of the density matrix $\hat{\rho}(t)$ according to the master equation (34). At $t = 0$ the system is assumed to be in a coherent state $|p = 1/2, q = 0\rangle$, i.e., a pure condensate with equal population and zero phase difference between the two wells. In the course of time, the Husimi function spreads and thus the coherence factor $\alpha(t) = \frac{2}{N} \langle \hat{J}_x \rangle_t$ decays as shown in part (b) of the figures.

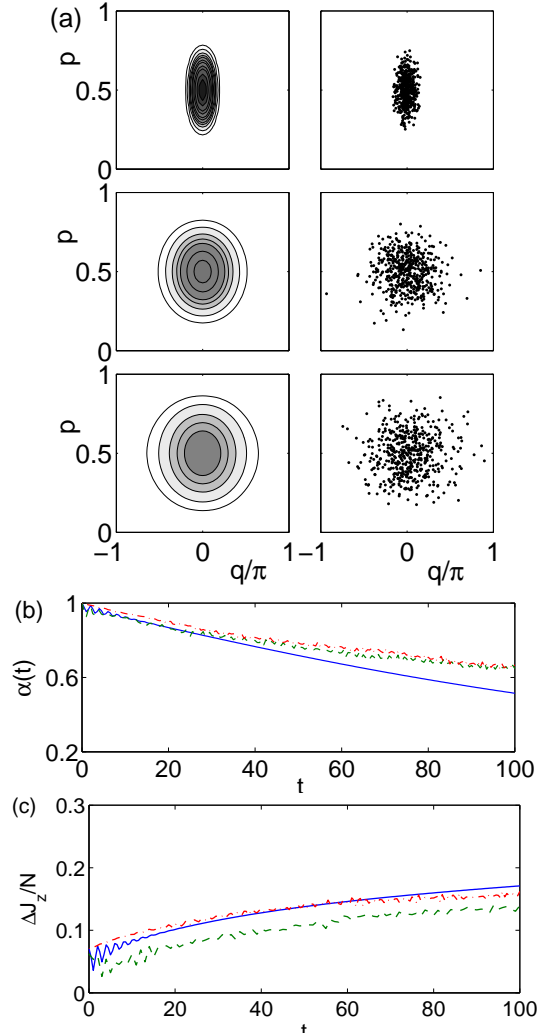


FIG. 19: (Color online) As Fig. 18, however for $UN = 10$.

The right-hand sides of Fig. 18(a) and Fig. 19(a) show the evolution of a classical phase space ensemble initially distributed according to the Husimi function $Q(p, q, 0)$. The single trajectories evolve according to the stochastic equations of motion (38) and thus diffuse over the classical phase space. One observes that the quantum dynamics is well reproduced by the classical approach, especially the different shape of the Husimi function for $U = 0$ and $UN = 10$ after the diffusion process.

For a more quantitative analysis we have plotted the coherence factor $\alpha(t)$ as well as the fluctuations of the population imbalance in Fig. 18 and Fig. 19. The quantum result $\frac{2}{N} \langle \hat{J}_x \rangle_t$ is compared to the ensemble averages (20) over 500 classical trajectories for the Q -function and P -function, respectively. In the linear case $UN = 0$ the mapping to stochastic evolution equations is exact and thus the deviations only result from the finite number of classical representations. For $UN = 10$, however, quantum noise is neglected leading to a systematic underestimation of loss of phase coherence.

Furthermore one observes that the coherence factor $\alpha(t)$ decreases much slower for $UN = 10$ compared to the non-interacting case $UN = 0$ both in the exact and in the classical calculation. Similarly, the fluctuations of the population imbalance grow much slower in the interacting case. These differences are readily understood from the structure of the classical phase space as shown in Fig. 3. One observes that the minimum of the classical Hamiltonian function $\mathcal{H}(p, q)$ is much deeper for $UN = 10$, so that the classical trajectories are bound much stronger and phase diffusion is significantly reduced (cf. also [36]). In addition, this leads to a stronger restriction of the phase space distribution in the J_z -axis.

VII. COMPARISON TO OTHER MEAN-FIELD APPROACHES

In the preceding sections we have introduced the number-conserving phase space description of the Bose-Hubbard model. This approach provides a straightforward derivation of the (discrete) Gross-Pitaevskii (GP) equation in the macroscopic limit and allows to go beyond mean-field theory. In the following we compare this method to other approaches to derive a mean-field approximation. The most common ones are the Bogoliubov and related approximations which are discussed in detail in Sec. VII A. Phase space methods are also frequently used, however starting from Glauber coherent states in almost all cases. A detailed comparison of the number conserving and the Glauber phase space description is given in Sec. VII B. Furthermore a considerable amount of work has been devoted to a rigorous derivation of the GP energy functional and the GP dynamics in the macroscopic limit (see, e.g., [49])

A. Bogoliubov theory and related approaches

The most common method to derive the (discrete) GP equation is the Bogoliubov approach, taking the expectation value of the Heisenberg equation of motion for the annihilation operator [50]

$$i \frac{d}{dt} \langle \hat{a}_j \rangle = -J (\langle \hat{a}_{j-1} \rangle + \langle \hat{a}_{j+1} \rangle) + U \langle \hat{a}_j^\dagger \hat{a}_j \hat{a}_j \rangle \quad (40)$$

and truncating the correlation functions

$$\langle \hat{a}_j^\dagger \hat{a}_k \hat{a}_\ell \rangle \approx \langle \hat{a}_j^\dagger \rangle \langle \hat{a}_k \rangle \langle \hat{a}_\ell \rangle. \quad (41)$$

Quantum fluctuations are completely neglected in this equation. They can be calculated approximately with the Bogoliubov-de Gennes equations which linearize the equations of motion for \hat{a}_j around the mean-field approximation given by the GP equation [23, 51]. If the initial state is a pure BEC, it is thus possible to calculate expectation values to all orders and to infer the increase of the non-condensed atoms from the dynamical (in-)stability of

the GP equation [23]. However, this approximation includes no backreaction of the non-condensed atoms onto the condensate mode, so that this approximation is restricted to short times.

To overcome this problem, one has to truncate higher order expectations values at a later stage than in Eqn. (41),

$$\begin{aligned} \langle \hat{a}_j^\dagger \hat{a}_j \hat{a}_j \rangle &\approx \langle \hat{a}_j^\dagger \rangle \langle \hat{a}_k \hat{a}_\ell \rangle + \langle \hat{a}_j^\dagger \hat{a}_k \rangle \langle \hat{a}_\ell \rangle + \langle \hat{a}_j^\dagger \hat{a}_\ell \rangle \langle \hat{a}_k \rangle \\ &\quad - 2 \langle \hat{a}_j^\dagger \rangle \langle \hat{a}_k \rangle \langle \hat{a}_\ell \rangle, \end{aligned} \quad (42)$$

and to derive equations of motion for the correlation functions $\langle \hat{a}_j^\dagger \hat{a}_k \rangle$ and $\langle \hat{a}_j \hat{a}_k \rangle$. Depending on the fact if and to which extend anomalous terms are neglected the resulting models are known under the name Hartree-Fock-Bogoliubov (HFB), HFB-Popov or Griffin (see, e.g., [52] and references therein). However, all these methods face some characteristic difficulties which are direct consequences of the breaking of the $U(1)$ symmetry [53]. For instance, none of them conserves the total number of particles and, at the same time, allows for particle exchange between the condensate and the remaining modes.

To overcome these problems, Anglin, Vardi and Tikhonenkov proposed the Bogoliubov backreaction (BBR) method [26, 39, 53]. In contrast to the $U(1)$ symmetry breaking approaches, only the number conserving operators $\hat{E}_{jk} = \hat{a}_j^\dagger \hat{a}_k$ are taken into account. Again, equations of motion are calculated for the expectation values $\langle \hat{E}_{jk} \rangle$ and the correlation functions $\langle \hat{E}_{jk} \hat{E}_{\ell m} \rangle$, where higher order expectation values are truncated. Several numerical examples shown in [53] suggest that the BBR method provides a better approximation to the many-particle dynamics than HFB and its varieties.

But still, BBR is limited to the first two moments of the operators \hat{E}_{jk} . Higher order correlation functions are not defined at all. This is clearly different within the phase space description, which allows to approximate arbitrary momenta.

From a practical viewpoint, it is thus fair to say that the phase space method embodies the best of both worlds: As the Bogoliubov-de Gennes approximation, it allows the calculation of expectation values to all orders and links the increase of the non-condensed atoms to the dynamical stability of the 'classical' GP equation. However, it also describes the depletion of the condensate mode and the long time dynamics just as the HFB and the BBR method. Last but not least it is even simpler to use and implement than both of them.

B. Comparison to $U(1)$ -symmetry breaking methods

Quantum phase space descriptions are usually based on the celebrated Glauber coherent states, which are superpositions of different number states. In particular, the dynamics of ultracold atoms in optical lattices has

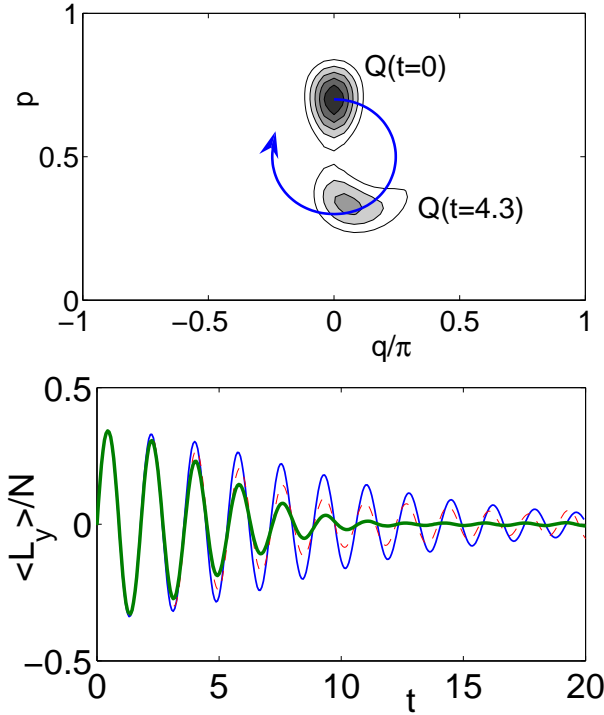


FIG. 20: (Color online) Dephasing of an initially coherent state. Upper panel: Illustration of the dynamics of the $SU(2)$ -Husimi function. Lower panel: Dynamics of the expectation value $\langle \hat{L}_y \rangle / N$ calculated exactly (solid blue line) and quasi-classically from an $SU(2)$ -Husimi distributed phase space ensemble (dashed red line) and a Glauber-Husimi distributed ensemble (thick green line).

been discussed in [24]. While this description is natural in quantum optics, where the birth and death of photons have to be taken into account, it does not take into account the $SU(M)$ symmetry of the Bose-Hubbard Hamiltonian. In this section, we will show that the number conserving description is superior in describing a BEC with a fixed number of particles. Note, however, that the $SU(M)$ symmetry is explicitly broken in the Gutzwiller approximation so that Glauber states provide the correct starting point in this case [25]. In this approximation, one considers only a single lattice site which couples to the mean-field on the remaining lattice sites so that the local particle number is not conserved any longer.

The $U(1)$ symmetry breaking phase space description is based on the Glauber coherent states

$$|\alpha_1, \alpha_2\rangle = e^{-(|\alpha_1|^2 + |\alpha_2|^2)/2} \sum_{n_1, n_2=0}^{\infty} \frac{\alpha_1^{n_1} \alpha_2^{n_2}}{\sqrt{n_1! n_2!}} |n_1, n_2\rangle, \quad (43)$$

where the particle number follows a Poissonian distribution. Let us briefly discuss the relation between the phase space representations based on $SU(2)$ and Glauber coherent states.

The Glauber coherent states (43) can be decomposed

as

$$|\alpha_1, \alpha_2\rangle = e^{-\frac{\alpha^2}{2}} \sum_{N=0}^{\infty} \frac{\alpha^N e^{-i\chi N}}{\sqrt{N!}} |p, q\rangle_N. \quad (44)$$

into $SU(2)$ coherent states with different particle numbers N , where the respective parameters are related by

$$\alpha_1 = \alpha e^{i\chi} \sqrt{p} \quad \text{and} \quad \alpha_2 = \alpha e^{i\chi} \sqrt{1-p} e^{-iq}. \quad (45)$$

Thus, α is the amplitude and χ is the global phase of the Glauber coherent state. Using this decomposition one can easily relate the Husimi functions based on $SU(2)$ coherent states and Glauber states. Consider an arbitrary many-particle quantum state $\hat{\rho}$ with N particles, which is represented by the $SU(2)$ Husimi function $Q_N(p, q)$. The Husimi function in terms of Glauber states is then given by

$$\begin{aligned} Q_{\text{Glauber}}(\alpha_1, \alpha_2) &= \langle \alpha_1, \alpha_2 | \hat{\rho} | \alpha_1, \alpha_2 \rangle \\ &= \frac{e^{-\alpha^2} \alpha^{2N}}{N!} Q_N(p, q) \end{aligned} \quad (46)$$

The physical implications of this mapping are clear: First of all, the Glauber-Husimi representation introduces artificial amplitude noise, since $|\alpha_1|^2 + |\alpha_2|^2 = \alpha^2$ is not fixed but Poisson-distributed. The dynamical effects of this will be discussed below. The classical phase space is then given by \mathbb{C}^2 and the distribution functions thus depend on four variables. In comparison, the approach based on the $SU(2)$ coherent states has some conceptual advantages as it directly embodies the conservation of the particle number N and eliminates the global phase χ . While the particle number is an operator in the $U(1)$ -symmetry breaking approach, it is a parameter in the $SU(2)$ mapping. Thus, the discussion of the macroscopic limit is much simplified, as well as the estimation of the error, which vanishes as $\mathcal{O}(1/N)$. Another approach discussing the convergence to the mean-field approximation by an expansion in terms of the inverse particle number $1/N$ has been used in [22, 23].

The effects of the artificial amplitude fluctuations can be quite significant. Let us illustrate them with a simple example shown in Fig. 20. We consider the dynamics of an $SU(2)$ coherent state located at $(p, q) = (0.7, 0)$ at $t = 0$ for $\Delta = 1$, $U = 0.1$ and $N = 50$ particles. This state then rotates around the elliptic fixed point of the classical dynamics at $(p, q) = (0.5, 0)$ and so the expectation values of the angular momentum operators (3) oscillate. These oscillations, however, are subject to dephasing and damping because of the quantum fluctuations of the initial state. Fig. 20 shows the dynamics of $s_y = \langle \hat{L}_y \rangle / N$ calculated exactly (solid blue line) and quasi-classically by the propagation of classical phase space ensembles. The ensembles were distributed according to the $SU(2)$ Husimi function (dashed red line) and the Glauber-Husimi function (46) (thick green line). While the damping is well reproduced by the $SU(2)$ ensemble, the artificial amplitude fluctuations

of the Glauber-Husimi ensemble cause significant deviations. This is due to the fact that the oscillation frequency around the elliptic fixed point strongly depends on the effective nonlinearity $U\alpha$ and thus trajectories with different normalization α dephase rapidly.

Moreover, already the description of a BEC in terms of $U(1)$ -symmetry breaking states reveals some ambiguities. For instance, consider an $SU(2)$ coherent state, representing a pure BEC. In the framework of the number-conserving phase space description, the P -representation of this state is simply a delta function. On the contrary, the P -function in terms of Glauber coherent states is strongly singular, including higher-order derivatives of the delta-function. A pure BEC with a fixed number of particles is thus the most classical state within the $SU(2)$ phase space description whereas it is highly non-classical in terms of the common Glauber phase space picture. In the first case an ensemble representation yields no dephasing at all while such a mapping is simply impossible in the latter case.

An extended and much more detailed overview over many different approaches to describe weakly-interacting condensates at finite, as well as at zero temperature is given in [54], including symmetry-breaking methods, as well as number conserving approaches. In this terminology, the method presented here can be seen as a combination of a stochastic phase space description with the number conserving approach.

VIII. CONCLUSION AND OUTLOOK

In the present paper we have discussed the number-conserving phase space description of small Bose-Hubbard systems and their generalization to an open quantum system. Apart from their theoretic value these systems have attracted considerable experimental interest within the last years, especially the two-mode case and its open counterpart [7, 9].

We have demonstrated the advantages of the (anti)-normal ordered quasi phase space densities based on the $SU(M)$ coherent states instead of the common Glauber states for the analysis and discussion of quantum states and especially of their dynamics. These representations allow a straightforward comparison of the many-body quantum system and its macroscopic counterpart given by the celebrated Gross-Pitaevskii equation. For instance the quantum eigenstates localize on the classical phase space trajectories. Moreover, we have presented an intuitive way to go beyond the usual mean-field limit: Considering the macroscopic limit $N \rightarrow \infty$ with $g = UN$ without assuming a maximally localized state yields a classical Liouvillian flow for the time evolution of the quasi-probability density or, equivalently, Monte Carlo ensembles of phase space trajectories. In contrast to the usual dynamics described by the GPE, this approach enables us to take into account arbitrary initial states and to estimate quantities depending on higher moments of

the quantum state. Obviously this also holds for larger lattices, for which a simulation of the full many-body dynamics is hard.

As an example for the extended scope of application, we consider a BEC approaching a classically unstable fixed point. The condensate fraction rapidly decreases so that the dynamics cannot be described by a single GPE-trajectory any longer. This failure has been denoted as the breakdown of the mean-field approximation in the literature [26, 39]. However, this breakdown is resolved using the Liouville dynamics, which provides a quite reasonable approximation for higher moments. Thus, in contrast to the common mean-field approach, it can also be used to describe and analyse chaotic systems. To underline this point, we study a driven two-mode system, as well as the dynamics of the three-mode case, which features an interesting transition from a regular to a mixed chaotic system, depending on the interaction strength. A comparison to exact results shows an excellent agreement with the Liouville dynamics, while the common mean-field dynamics strongly diverge from the exact results and fail to describe the effects of the dynamical instability. Moreover, the approximation of higher moments via the Liouville dynamics allows to investigate many interesting quantities, like the single particle density matrix and the condensate fraction, which are not accessible within the common approach. To underline this point, we study the depletion and the heating of the condensate.

In the last chapter, we give an overview over different methods, which can be used to derive mean-field systems and their possible extensions and relate these to the approach presented here. Special attention is paid upon the comparison to methods based on $U(1)$ -symmetry breaking Glauber states and the implications of the conservation of the total particle number. We show that even for simple examples the artificial noise in the particle number can result in larger deviations appearing on a much shorter time scale compared to the approach presented here. Moreover, ambiguities in the description of macroscopic states and the set of problems considering the macroscopic limit with \hat{N} being an operator can be tackled easily in the number conserving description where N is simply a parameter. This completes the formal comparison of different possibilities of trial states in [27, 55]. Note, however, that the benefits of a description based on generalized coherent states are not restricted to dynamical problems, see e.g. the semiclassical description of the ground state [56] and the excitation spectrum based on $SU(M)$ coherent states [55, 57].

The introduction of generalized coherent states and the corresponding phase space distributions opens the door for the use of semiclassical methods for the analysis of the dynamics of the Bose-Hubbard model. The Liouville approach is of course not capable to describe generic quantum effects such as tunneling in quantum phase space and (self-)interference. These features can be reconstructed using semiclassical coherent state propagators (see, e.g. [58, 59] and references therein). In the first

part of the present work [6] we have introduced the phase space description and calculated the equations of motion for an arbitrary number of modes. The generalization of the ensemble method to this case is straightforward and allows the approximate calculation of many-particle quantities such as the condensate fraction or higher moments with small numerical efforts. Concrete applications to larger systems, as well as an extended study of the three-mode system will be subject of a future paper.

Moreover, the analysis of the mean-field dynamics has only recently been proven to be extremely useful for the understanding of the role of noise in two-mode Bose-Hubbard systems which face many theoretically and experimentally interesting features, like e.g. a stochastic

resonance effect [44, 45]. However, very little is known about the behaviour of larger dissipative systems, where the presented methods could provide an illustrative and easily implementable tool.

Acknowledgments

Support from the Studienstiftung des deutschen Volkes and the German Research Foundation (DFG) through the Graduiertenkolleg 792 and the research fellowship program (grant number WI 3415/1) is gratefully acknowledged.

-
- [1] M. P. A. Fisher, P. B. Weichman, G. Grinstein, and D. S. Fisher, *Phys. Rev. B* **40**, 546 (1989).
- [2] C. J. Pethick and H. Smith, *Bose-Einstein Condensation in Dilute Gases* (Cambridge University Press, Cambridge, 2008).
- [3] C. Brif and A. Mann, *Phys. Rev. A* **59**, 971 (1999).
- [4] W.-M. Zhang, D. H. Feng, and R. Gilmore, *Rev. Mod. Phys.* **62**, 867 (1990).
- [5] A. M. Perelomov, *Generalized Coherent States and Their Applications* (Springer, Berlin Heidelberg New York London Paris Tokyo, 1986).
- [6] F. Trimborn, D. Witthaut, and H. J. Korsch, *Phys. Rev. A* **77**, 043631 (2008).
- [7] M. Albiez, R. Gati, J. Fölling, S. Hunsmann, M. Cristiani, and M. K. Oberthaler, *Phys. Rev. Lett.* **95**, 010402 (2005).
- [8] T. Schumm, S. Hofferberth, L. M. Andersson, S. Wildermuth, S. Groth, I. Bar-Joseph, J. Schmiedmayer, and P. Krüger, *Nature Physics* **1**, 57 (2005).
- [9] R. Gati, B. Hemmerling, J. Fölling, M. Albiez, and M. K. Oberthaler, *Phys. Rev. Lett.* **96**, 130404 (2006).
- [10] S. Fölling, S. Trotzky, P. Cheinet, M. Feld, R. Saers, A. Widera, T. Müller, and I. Bloch, *Nature* **448**, 1029 (2007).
- [11] C. Orzel, A. K. Tuchman, M. L. Fenselau, M. Yasuda, and M. A. Kasevich, *Science* **291**, 2386 (2001).
- [12] Biao Wu and Qian Niu, *Phys. Rev. A* **61**, 023402 (2000).
- [13] D. Witthaut, E. M. Graefe, and H. J. Korsch, *Phys. Rev. A* **73**, 063609 (2006).
- [14] G. J. Milburn, J. Corney, E. M. Wright, and D. F. Walls, *Phys. Rev. A* **55**, 4318 (1997).
- [15] A. Smerzi, S. Fantoni, S. Giovanazzi, and S. R. Shenoy, *Phys. Rev. Lett.* **79**, 4950 (1997).
- [16] S. Raghavan, A. Smerzi, S. Fantoni, and S. R. Shenoy, *Phys. Rev. A* **59**, 620 (1999).
- [17] J. Estève, C. Gross, A. Weller, S. Giovanazzi, and M. K. Oberthaler, *Nature* (2008).
- [18] P. Buonsante, R. Franzosi, and V. Penna, *Phys. Rev. Lett.* **90**, 050404 (2003).
- [19] R. Franzosi and V. Penna, *Phys. Rev. E* **67**, 046227 (2003).
- [20] E. M. Graefe, H. J. Korsch, and D. Witthaut, *Phys. Rev. A* **73**, 013617 (2006).
- [21] S. Mossmann and C. Jung, *Phys. Rev. A* **74**, 033601 (2006).
- [22] Y. Castin and R. Dum, *Phys. Rev. Lett.* **79**, 3553 (1997).
- [23] Y. Castin and R. Dum, *Phys. Rev. A* **57**, 3008 (1998).
- [24] M. J. Steel, M. K. Olsen, L. I. Plimak, P. D. Drummond, S. M. Tan, M. J. Collett, D. F. Walls, and R. Graham, *Phys. Rev. A* **58**, 4824 (1998).
- [25] P. Jain and C. W. Gardiner, *J. Phys. B* **37**, 3649 (2004).
- [26] A. Vardi and J. R. Anglin, *Phys. Rev. Lett.* **86**, 568 (2001).
- [27] P. Buonsante and V. Penna, *J. Phys. A* **41**, 175301 (2008).
- [28] K. Nemoto and B. C. Sanders, *J. Phys. A* **34**, 2051 (2001).
- [29] K. Nemoto, *J. Phys. A* **33**, 3493 (2000).
- [30] K. Nemoto, C. A. Holmes, G. J. Milburn, and W. J. Munro, *Phys. Rev. A* **63**, 013604 (2000).
- [31] C. Lee, T. J. Alexander, and Y. S. Kivshar, *Phys. Rev. Lett.* **97**, 180408 (2006).
- [32] R. Franzosi and V. Penna, *Phys. Rev. A* **65**, 013601 (2001).
- [33] A. B. Klimov, *J. Math. Phys.* **43**, 2202 (2002).
- [34] D. Zueco and I. Calvo, *J. Phys. A* **40**, 4635 (2007).
- [35] D. W. Barry and P. D. Drummond, *Phys. Rev. A* (in print), preprint arXiv:0808.2226.
- [36] G.-B. Jo, Y. Shin, S. Will, T. A. Pasquini, M. Saba, W. Ketterle, D. E. Pritchard, M. Vengalattore, and M. Prentiss, *Phys. Rev. Lett.* **98**, 030407 (2007).
- [37] S. Gnutzmann and K. Zyczkowski, *J. Phys. A* **34**, 10123 (2001).
- [38] G. J. Milburn, R. Laflamme, B. C. Sanders, and E. Knill, *Phys. Rev. A* **65**, 032316 (2002).
- [39] J. R. Anglin and A. Vardi, *Phys. Rev. A* **64**, 013605 (2001).
- [40] H. Zhong, W. Hai, and S. Rong, *J. Phys. B: At. Mol. Opt. Phys.* **41**, 175301 (2008).
- [41] A. Sørensen, L.-M. Duan, I. Cirac, and P. Zoller, *Nature* **409**, 63 (2003).
- [42] A. J. Leggett, *Rev. Mod. Phys.* **73**, 307 (2001).
- [43] R. Gati, J. Esteve, B. Hemmerling, T.B. Ottenstein, J. Appmeier, A. Weller, and M. K. Oberthaler, *New J. Phys.* **8**, 189 (2006).
- [44] F. Trimborn, D. Witthaut, and S. Wimberger, *J. Phys. B: At. Mol. Opt. Phys.* **41**, 171001 (FTC) (2008)
- [45] F. Trimborn, D. Witthaut, and S. Wimberger, accepted

- by Phys. Rev. Lett., preprint: arXiv:0809.1776 (2008).
- [46] J. Anglin, Phys. Rev. Lett. **79**, 6 (1997).
 - [47] J. Ruostekoski and D. F. Walls, Phys. Rev. A **58**, R50 (1998).
 - [48] D. F. Walls and G. J. Milburn, Phys. Rev. A **31**, 2403 (1985).
 - [49] E. H. Lieb, R. Seiringer, and J. Yngvason, Phys. Rev. A **61**, 043602 (2000).
 - [50] N. N. Bogoliubov, J. Phys. (USSR) **11**, 23 (1947).
 - [51] C. W. Gardiner, Phys. Rev. A **56**, 1414 (1997).
 - [52] A. Griffin, Phys. Rev. B **53**, 9341 (1996).
 - [53] I. Tikhonenkov, J. R. Anglin, and A. Vardi, Phys. Rev. A **75**, 013613 (2007).
 - [54] N. P. Proukakis and B. Jackson, J. Phys. B: At. Mol. Opt. Phys. **41**, 203002 (2008).
 - [55] R. Franzosi, V. Penna, and R. Zecchina, Int. J. Mod. Phys. B **14**, 943 (2000).
 - [56] P. Buonsante, V. Penna, and A. Vezzani, Phys. Rev. A **72**, 043620 (2005).
 - [57] R. Franzosi and V. Penna, Phys. Rev. A **63**, 043609 (2001).
 - [58] M. Stone, K.-S. Park, and A. Garg, J. Math. Phys. **41**, 8025 (2000).
 - [59] M. Baranger, M. A. M. de Aguiar, F. Keck, H. J. Korsch, and B. Schellhaaß, J. Phys. A **34**, 7227 (2001).